



# Dual-phase cobalt phosphide/phosphate hybrid interactions via iridium nanocluster interfacial engineering toward efficient overall seawater splitting

Van Hien Hoa<sup>a</sup>, Muthu Austeria<sup>a</sup>, Huyen Thi Dao<sup>b</sup>, Mai Mai<sup>b</sup>, Do Hwan Kim<sup>b,\*</sup>

<sup>a</sup> Department of Nano Convergence Engineering, Jeonbuk National University, Jeonju, Jeonbuk 54896, Republic of Korea

<sup>b</sup> Division of Science Education, Graduate School of the Department of Energy Storage/Conversion Engineering, Jeonbuk National University, Jeonju, Jeonbuk 54896, Republic of Korea

## ARTICLE INFO

### Keywords:

Co<sub>2</sub>P/Co<sub>2</sub>P<sub>2</sub>O<sub>7</sub>  
Interfacial engineering  
Iridium nanocluster  
Seawater splitting

## ABSTRACT

Surface engineering and electronic modification are the two primary elements for improving the catalytic properties of electrode materials. We significantly improved the catalytic performances of interfacial-engineered Ir nanocluster-containing cobalt phosphide/phosphate heterostructured nanowires on nickel foam (Ir-Co<sub>2</sub>P/Co<sub>2</sub>P<sub>2</sub>O<sub>7</sub> NWs/NF) in water splitting. The optimized Ir nanocluster content of 0.05 wt% resulted in a highly efficient catalytic performance, significantly outperforming commercial IrO<sub>2</sub> and Pt-C catalysts. The Ir<sub>0.05</sub>-Co<sub>2</sub>P/Co<sub>2</sub>P<sub>2</sub>O<sub>7</sub> NW bifunctional electrocatalyst displayed cell potentials of 1.52, 1.60, 1.62, and 1.67 V in 1.0 M KOH and mimic, simulated, and natural seawater, respectively, at 10 mA cm<sup>-2</sup>. DFT analysis confirmed that the heterostructure enrichment in the z-oriented d-orbital facilitates strong electronic interactions between the adsorbates and surfaces. The keys were the simultaneous generation of metal phosphide/phosphate via activation of the P site on the support. Furthermore, the electrocatalyst exhibited a solar-to-hydrogen efficiency of 22.4% in solar energy-aided water splitting, indicating that it is a viable, inexpensive candidate for use in water splitting.

## 1. Introduction

The oceans hold approximately 96.5% of the global water supply, and seawater (SW) splitting provides infinite hydrogen with zero CO<sub>2</sub> emissions while placing little strain on the global freshwater supply [1]. Furthermore, hydrogen production via solar-driven electrochemical water splitting may be the optimal route because of its suitability, cheap, and green nature [2,3]. However, the negative effects of ionic poisoning, corrosion, and side reactions on cell performance pose additional challenges in the electrolysis of SW with complex ionic chemistry [4]. Under alkaline conditions, the chlorine evolution reaction (CLER) may be suppressed by maintaining the overpotential of the oxygen evolution reaction (OER) at < 0.48 V [5]. Furthermore, the use of catalytic

powders necessitates the utilization of a coating containing a nonconducting polymeric binder, which limits the number of active sites and charge transfer, thereby deteriorating the catalytic performance and significantly limiting the large-scale applications [6]. Currently, the commercial benchmark Pt-C electrocatalyst is used in the hydrogen evolution reaction (HER), and RuO<sub>2</sub> or IrO<sub>2</sub> is used in the OER [7,8], but their increasing costs and scarcities significantly limit their widespread applications. Therefore, developing low-cost, efficient, stable bifunctional water-splitting catalysts using earth-abundant metals is essential [9,10]. To date, the reported critical factors that may tune catalyst activity toward the overall water splitting include crystal defects, morphology, metal-nonmetal hybridization, heteroatom doping, alloying, and metal construction within graphitic layered materials [11–13].

**Abbreviations:** BET, Brunauer–Emmett–Teller; CLER, chlorine evolution reaction; DFT, density functional theory; DI, deionized; DOS, density of states; ECSA, electrochemical active surface area; EDS, energy-dispersive X-ray spectroscopy; EIS, electrochemical impedance spectroscopy; HAADF-STEM, high-angle annular dark-field scanning transmission electron microscopy; HAABF-STEM, high-angle annular bright-field scanning transmission electron microscopy; HER, hydrogen evolution reaction; HR-TEM, high-resolution transmission electron microscopy; ICP-OES, inductively coupled plasma optical emission spectrometry; LSV, linear sweep voltammetry; NF, Ni foam; NP, nanoparticle; NW, nanowire; OER, oxygen evolution reaction; SA, single atom; SEM, scanning electron microscopy; STH, solar-to-hydrogen; SW, seawater; TEM, transmission electron microscopy; TM, transition metal; XPS, X-ray photoelectron spectroscopy; XRD, X-ray diffraction.

\* Corresponding author.

E-mail address: [dhk201@jbnu.ac.kr](mailto:dhk201@jbnu.ac.kr) (D.H. Kim).

<https://doi.org/10.1016/j.apcatb.2023.122467>

Received 30 August 2022; Received in revised form 8 January 2023; Accepted 11 February 2023

Available online 12 February 2023

0926-3373/© 2023 Elsevier B.V. All rights reserved.

Transition metal (TM) phosphides, selenides, sulfides, nitrides, carbides, and TMs within graphitic layers have been reported as water-splitting electrocatalysts [14]. TM phosphates and phosphides are the most effective catalytic agents in the OER and HER, respectively [6,15]. TM phosphides exhibit the most promising catalytic HER performances because their hydrogen adsorption Gibbs energies ( $\Delta G_{H^+}$ ) are similar to those of Pt-based catalysts [6]. P atoms are negatively charged when doped into TM crystal lattices because they have higher electronegativities than the transition metal atoms [16,17]. These negatively charged P atoms are essential in the initial Volmer stage of the HER ( $H^+$  adsorption on the active site). However, TM phosphates exhibit superior catalytic properties, high durabilities, and unique OER capacities [18–20]. In comparison to single-phase or single-crystal catalytic materials, the coexistence of several crystalline phase/components to form a heterostructure linked by a well-defined interface causes electronic modulation and lattice tension. These effects lower the reaction barrier, increase the type/number of catalytic sites, and promote charge transfer, thereby improving the electrocatalytic activity in  $H_2$  production synergistically [21]. Heterostructured cobalt phosphide/phosphate, which is a well-known earth-abundant catalyst of overall water splitting that self-assembles from multi-crystal phosphides and phosphates, exhibits excellent stability and catalytic activity over a broad pH range of 0–14 [22–24]. In addition, with material advancements, it is a promising bifunctional SW splitting catalyst with excellent performance. A conducting substrate, such as Ni foam (NF), is typically used to accelerate electron transfer, avoid agglomeration, and increase the exposed active sites, allowing for high activity and strength during long-term electrolysis [25]. Furthermore, incorporating intermediate TMs, such as single atoms (SAs) and nanoclusters and -particles, into heterostructures is a prospective strategy to increase electrode stability and reduce the overpotential in bifunctional water splitting [26]. Although SAs exhibit remarkable properties, their industrial applications are frequently hindered by their low concentrations on substrates [27]. Small metal nanoclusters provide active sites for novel catalysts due to their diverse atomic packing structures and quantized electronic states [28–31]. Based on the experimental and theoretical volcano relationships of the HER and OER, a hybrid of interconnected Ir and phosphide/phosphate may be a promising bifunctional catalyst for water splitting. This is because the binding energy between the reactant and catalyst is very close to the vertices of both volcanoes (Sabatier principle) [32–34]. The formation of a heterostructure with Ir and foreign atoms results in a coordination effect, which shifts the  $d$ -orbital center, and the adsorbate directly influences the  $d$ -band surface energy [16,35]. We thus developed a powerful, durable bifunctional electrocatalyst with uniformly dispersed, ultrafine interfaces engineered to tune the electronic configuration and states and accelerate electron and ion transport, resulting in effective synergistic effects that enhance its water-splitting performance. The dual phase of cobalt phosphide/phosphate hybrid interactions, Ir nanocluster interfacial engineering, and the enhancement in the  $z$ -oriented  $d$ -orbitals facilitated electronic interactions between the adsorbates and surfaces. The Ir within the hybrid not only enhanced electron transfer but also promoted the OER. As a free-standing electrode, the synthesized Ir nanocluster-containing cobalt phosphide/phosphate heterostructured nanowires (NWs) on the NF catalyst outperformed most of the reported cutting-edge OER and HER catalysts. Our catalyst displayed an outstanding mass activity that outperformed the benchmark marketable Pt/C,  $IrO_2$  catalysts, serving as a promising candidate for use in state-of-the-art  $H_2$  generation via SW splitting.

## 2. Experimental

### 2.1. Synthesis of the $Ir-Co_2P/Co_2P_2O_7$ NWs on NF

To remove surface oxides, NF in the size of  $2 \times 3$  cm was treated with acetone, ethanol, HCl (3.0 M), and deionized (DI) water prior to use as a substrate. The Co precursor was synthesized by hydrothermally reacting

2 mmol  $Co(NO_3)_2 \cdot 6H_2O$  and 20 mmol urea in 50 mL of DI water for 6 h at  $120^\circ C$  to yield Co-OH NWs on the NF. The product was then impregnated with Ir via immersion in an aqueous solution containing 0.01, 0.05, 0.1, or 1.0 mM  $IrCl_3 \cdot xH_2O$  for 1 h [36]. The produced Ir-Co-OH NWs were placed in the furnace with  $NaH_2PO_2$  as a source of P and annealed from  $25^\circ$  to  $350^\circ C$  at  $3^\circ C/min$  under an Argon flow of  $120 mL min^{-1}$ . After the reaction was completed, the sample was then cooled to ambient temperature for characterization of the  $Ir-Co_2P/Co_2P_2O_7$  NWs. Further,  $Co_2P/Co_2P_2O_7$  NWs were prepared using the same procedure, without using  $IrCl_3 \cdot xH_2O$ .

## 3. Results and discussion

### 3.1. Morphology and structural analysis

Fig. 1a shows a schematic diagram of the preparation of Ir decorated cobalt phosphide/phosphate. The surface morphology of the catalyst was examined using field emission scanning electron microscopy (SEM). The SEM images reveal uniform Co-OH NWs with diameters of approximately 60 nm that are bottom-up assembled extremely regularly on the NF. They are thus linked to form a continuous network, which facilitates high porosity and effective Ir-center dispersion (Fig. S1). Following fabrication via the hydrothermal reaction, the Ir-Co-OH NWs may be synthesized via the spontaneous galvanic displacement of Co-OH by Ir ions in the reaction between Co-OH and the Ir precursor (Fig. S2) [37]. Ir is impregnated into the Co-OH NWs for 1 h using the  $IrCl_3 \cdot xH_2O$  precursor solutions, followed by phosphidation at  $350^\circ C$  using  $NaH_2PO_2$  [38]. The release of  $PH_3$  and  $H_2$  via the disproportionation of  $NaH_2PO_2$  drives the phosphidation of the parent oxides, and  $H_2$  is produced by the reaction of metal oxides and  $PH_3$  [39]. Extending the annealing time or using a higher temperature may induce the conversion from cobalt phosphide to the corresponding phosphate in a moist environment, where  $H_2O$  is derived from the previous reaction. Furthermore, if the phosphide is produced at high temperature, the Co-P may condense further to polyphosphates. When the phosphide/phosphate heterostructure is successfully fabricated, it may have a heterogeneous interfacial structure with an increased number and type of active sites, along with rapid charge transfer, resulting in synergistic effects to improve catalytic performance [39]. The morphologies of the  $Co_2P/Co_2P_2O_7$  NWs after phosphidation perfectly retain their original NW characteristics, with smooth outer surfaces and sharp tips (Fig. 1b–d). Furthermore, the morphologies of the  $Ir-Co_2P/Co_2P_2O_7$  NWs were modified by controlling the concentration of  $IrCl_3 \cdot xH_2O$  used. At a high magnification, the surfaces of the  $Ir-Co_2P/Co_2P_2O_7$  NWs prepared using 0.01 mM  $IrCl_3 \cdot xH_2O$  are shiny (Fig. 1e), similar to those of the sample without Ir. However, Fig. 1f shows that the surfaces of the  $Ir-Co_2P/Co_2P_2O_7$  NWs prepared using 0.05 mM  $IrCl_3 \cdot xH_2O$  retain their uniform sizes but are relatively rough. Therefore, the presence of a few nanoparticles (NPs), resulting in extreme roughness, or numerous NPs, resulting in uniform decoration, upon using a  $IrCl_3 \cdot xH_2O$  concentration of 0.1–1.0 mM suggests that a higher  $IrCl_3 \cdot xH_2O$  concentration may cause NP formation (Fig. 1g and S2). The Ir atoms of Ir-O-Co aggregate to form nanoclusters or NPs on the surface of the phosphide/phosphate phase [30,40]. Fig. S3 also shows that the use of an increasing concentration of 0.01, 0.05, 0.1, or 1.0 mM  $IrCl_3 \cdot xH_2O$  generally increases the sizes of the Ir NPs and their surface coverage, which is attributed to particle growth. Figs. S3e–f show the statistical distributions, with the Ir NPs of the samples prepared using 0.1 and 1 mM  $IrCl_3 \cdot xH_2O$  exhibiting average diameters of 7.9 and 17 nm, respectively. These features of the Ir-hybrid, and the unique 1D nanoheterostructured assemblies on the NF that may be quite regular, increase the surface area with a large number of electroactive sites. The total amounts of Ir in the samples were determined by Inductively coupled plasma optical emission spectrometry (ICP-OES).

The  $Ir-Co_2P/Co_2P_2O_7$  NWs prepared using concentrations of 0.01, 0.05, 0.1, and 1.0 mM  $IrCl_3 \cdot xH_2O$  contain Ir contents of approximately

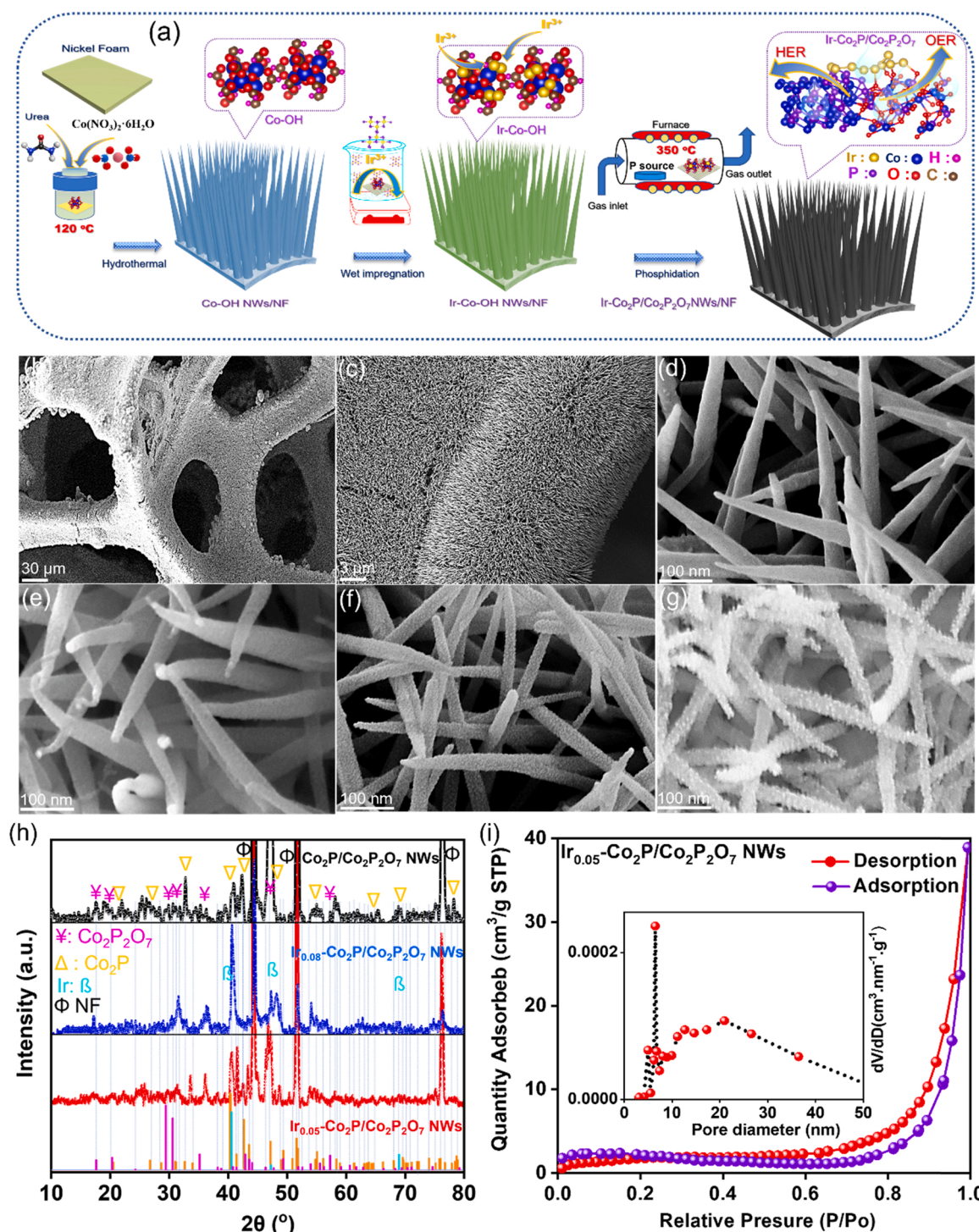


**Fig. 1.** (a) Schematic diagram of the manufacture of the  $\text{Ir-Co}_2\text{P/Co}_2\text{P}_2\text{O}_7$  nanowires (NWs), (b)–(d) scanning electron microscopy (SEM) images of the  $\text{Co}_2\text{P/Co}_2\text{P}_2\text{O}_7$  NWs, high-resolution SEM images of the  $\text{Ir-Co}_2\text{P/Co}_2\text{P}_2\text{O}_7$  NWs with (e) 0.04, (f) 0.05, or (g) 0.08 wt% Ir, (h) X-ray diffraction patterns of the  $\text{Co}_2\text{P/Co}_2\text{P}_2\text{O}_7$  NWs,  $\text{Ir}_{0.05}\text{-Co}_2\text{P/Co}_2\text{P}_2\text{O}_7$  NWs, and  $\text{Ir}_{0.08}\text{-Co}_2\text{P/Co}_2\text{P}_2\text{O}_7$  NWs (i) Brunauer–Emmett Teller isotherms and pore sizes of the  $\text{Ir}_{0.05}\text{-Co}_2\text{P/Co}_2\text{P}_2\text{O}_7$  NWs.

0.04 ( $\text{Ir}_{0.04}\text{-Co}_2\text{P/Co}_2\text{P}_2\text{O}_7$  NWs), 0.05 ( $\text{Ir}_{0.05}\text{-Co}_2\text{P/Co}_2\text{P}_2\text{O}_7$  NWs), and 0.08 ( $\text{Ir}_{0.08}\text{-Co}_2\text{P/Co}_2\text{P}_2\text{O}_7$  NWs) wt%, respectively (Table S1). This is attributed to the effective deposition of Ir on the surfaces of the  $\text{Co}_2\text{P/Co}_2\text{P}_2\text{O}_7$  NWs, significantly altering the micromorphologies and crystal structures, as demonstrated by SEM and transmission electron microscopy (TEM) images. Furthermore, the X-ray diffraction (XRD) patterns contain broad peaks at  $2\theta = 44.3^\circ$ ,  $51.6^\circ$ , and  $76.5^\circ$ , which respectively correspond to the  $d(111)$ ,  $d(200)$ , and  $d(220)$  planes of NF. Moreover, the sharp peaks at  $2\theta = 17.1^\circ$ ,  $19.6^\circ$ ,  $24.2^\circ$ ,  $26.8^\circ$ ,  $28.8^\circ$ ,  $33.4^\circ$ ,  $35.5^\circ$ ,

$39.2^\circ$ ,  $52.9^\circ$ ,  $59.9^\circ$ , and  $65.2^\circ$  may be indexed to the reflections of the (020), (001), (111), (220), (121), (221), (040), (301), (231), (060), and (450) planes, respectively, of the crystalline mixture of the  $\text{Co-OH}$  (JCPDS No. 48–0083) phase, as presented in Fig. S4. Furthermore, the XRD pattern of the  $\text{Ir-Co-OH}$  NWs (0.05 mM) shows small shifts and lower intensities compared to those of virgin  $\text{Co-OH}$  NWs, indicating the effects of surface decoration with Ir atoms. After phosphidation, the XRD patterns of the catalytic materials display numerous distinct peaks. The XRD pattern of  $\text{Co}_2\text{P/Co}_2\text{P}_2\text{O}_7$  NWs reveals dominant peaks at  $2\theta$



= 17.8°, 19.7°, 24.2°, 26.7°, 28.9°, 29.5°, 31.6°, 36.2°, 41.1°, 69.3°, and 70.0°, which may be assigned to the (020), (100), (021), (120), (111), (100), (283), (13–1), (102), (170), and (11–4) planes, respectively, of monoclinic  $\text{Co}_2\text{P}_2\text{O}_7$  (ICSD No. 59291). It also displays diffraction peaks at  $2\theta \approx 20.3^\circ$ ,  $26.6^\circ$ ,  $28.5^\circ$ ,  $30.9^\circ$ ,  $32.6^\circ$ ,  $33.9^\circ$ ,  $40.3^\circ$ ,  $40.4^\circ$ ,  $41.4^\circ$ ,  $42.7^\circ$ ,  $43.5^\circ$ ,  $47.8^\circ$ ,  $49.0^\circ$ ,  $49.4^\circ$ ,  $51.6^\circ$ ,  $51.8^\circ$ ,  $54.9^\circ$ ,  $55.1^\circ$ ,  $58.5^\circ$ ,  $70.6^\circ$ ,  $75.4^\circ$ , and  $78.9^\circ$ , which correspond to the characteristic (101), (022), (011), (102), (111), (201), (112), (210), (202), (211), (103), (013), (212), (310), (020), (203), (004), (302), (213), (410), (304), and (205) planes, respectively, of orthorhombic  $\text{Co}_2\text{P}$  (JCPDS No. 03–065–2381, Fig. 1h) [41,42]. Furthermore, the absence of specific diffraction peaks representing the Ir phase in the XRD pattern of the  $\text{Ir}_{0.05}\text{-Co}_2\text{P/Co}_2\text{P}_2\text{O}_7$  NWs is due to the small sizes and amounts of metallic Ir clusters (0.05 wt %) available on the phosphide/phosphate surface. Hence, the presence of Ir in this sample may not be clearly determined using XRD but is confirmed via X-ray photoelectron spectroscopy (XPS) and ICP-OES, as observed in previous studies [43]. Where atomic Ir is deposited on the

crystalline phosphide/phosphate phase, the intensities of the peaks at  $2\theta = 41.4^\circ$ ,  $42.7^\circ$ , and  $43.5^\circ$ , corresponding to the  $\text{Co}_2\text{P}$  phase, and  $2\theta = 41.1^\circ$ , corresponding to the  $\text{Co}_2\text{P}_2\text{O}_7$  phase, are reduced in the XRD pattern of the  $\text{Ir}_{0.05}\text{-Co}_2\text{P/Co}_2\text{P}_2\text{O}_7$  NWs. Additionally, broader shifts consistent with  $2\theta = 0.2^\circ$  are observed compared to the XRD pattern of the bare sample (Fig. S5). Thus, the XRD pattern of Ir (JCPDS No. 87–0715) embedded in a heterostructure displays a higher intensity peak at  $2\theta = 40.6^\circ$  than that detected in the XRD pattern of the  $\text{Ir}_{0.05}\text{-Co}_2\text{P/Co}_2\text{P}_2\text{O}_7$  NWs [44,45]. The results of XRD are consistent with the estimated average crystalline size of Ir of 7.9 nm, as shown in Fig. S3e. In addition, Brunauer–Emmett–Teller (BET) studies were conducted to measure the surface area of the  $\text{Ir}_{0.05}\text{-Co}_2\text{P/Co}_2\text{P}_2\text{O}_7$  NW material, based on adsorption-desorption isotherms, to investigate the effects of the porous properties (Fig. 1i). The BET surface area is  $9 \text{ m}^2 \text{ g}^{-1}$ , with a large pore volume and mesoporous size distribution (5–50 nm), which provided various pathways for charge transfer and fast ion diffusion during catalytic processes [38]. High-angle annular

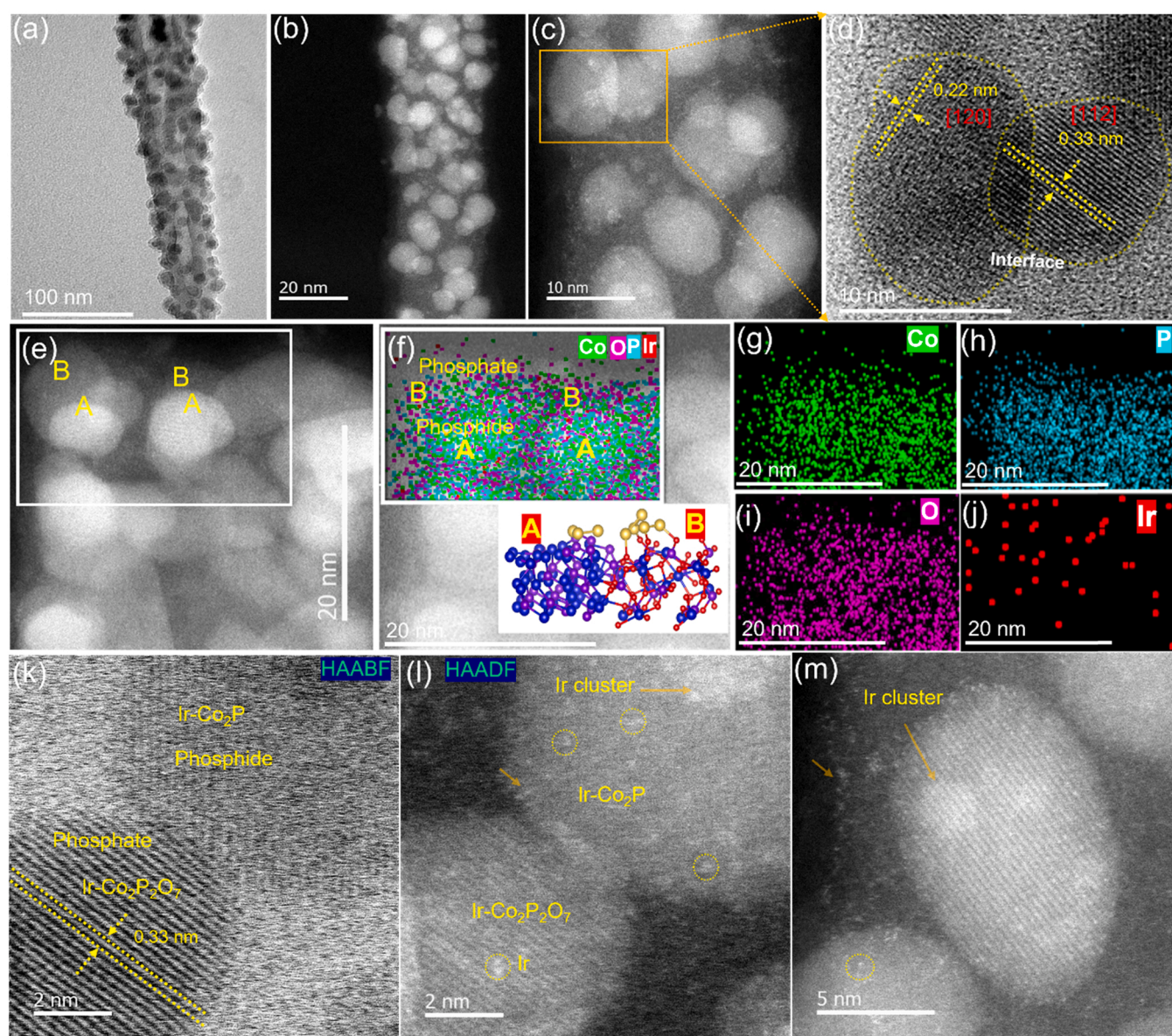


**Fig. 2.** (a) High-angle annular bright-field scanning transmission electron microscopy (HAABF-STEM) image of the  $\text{Ir}_{0.05}\text{-Co}_2\text{P/Co}_2\text{P}_2\text{O}_7$  nanowires (NWs), (b–c) high-angle annular dark-field STEM (HAADF-STEM) and (d) high-resolution TEM images of  $\text{Ir}_{0.05}\text{-Co}_2\text{P/Co}_2\text{P}_2\text{O}_7$ , (e) HAADF-STEM image of phosphide/phosphate particles corresponding to the (f) color mapping of (g) Co, (h) P, (i) O, and (j) Ir, (k) BF and (l) DF images of the  $\text{Ir}_{0.05}\text{-Co}_2\text{P/Co}_2\text{P}_2\text{O}_7$  NWs corresponding to Ir-Co<sub>2</sub>P and Ir-Co<sub>2</sub>P<sub>2</sub>O<sub>7</sub>, and (m) HAADF-STEM image of Ir atoms as bright dots dispersed on the hybrid materials.



dark-field scanning TEM (HAADF-STEM) and elemental mapping via energy-dispersive X-ray spectroscopy (EDS) were used to investigate the crystal structures. A TEM image of the  $\text{Co}_2\text{P}/\text{Co}_2\text{P}_2\text{O}_7$  NWs shows an individual NW with a hierarchical porous structure with a width of approximately 60 nm (Fig. S6a). High-resolution TEM (HR-TEM) reveals the quantity of small NPs at the heterostructured phosphide/phosphate interface in the framework, which are accompanied by the amorphous or crystalline form of the porous structure, as shown in Figs. S6b–c. According to the XRD patterns, the HR-TEM images show lattice fringes that correlate with  $d$ -spacings of  $d(112) = 0.22$  nm of  $\text{Co}_2\text{P}$  and  $d(120) = 0.33$  nm of  $\text{Co}_2\text{P}_2\text{O}_7$ , corresponding to the fast Fourier transform images.

Therefore, the structural configuration of the heterostructure is based on two distinct crystalline structures,  $\text{Co}_2\text{P}$  and  $\text{Co}_2\text{P}_2\text{O}_7$ . The high-angle annular bright-field (HAADF)-STEM image of the  $\text{Ir}_{0.05}\text{-Co}_2\text{P}/\text{Co}_2\text{P}_2\text{O}_7$  NWs reveals numerous ultrasmall nanocrystals uniformly decorating the entire NW (Fig. 2a). The HAADF image shown in Fig. 2b reveals the bright and dark colors representing the locations of the different phases within the hybrid, and the HR-TEM images show lattice fringes that correlate with the  $d$ -spacings of the  $\text{Co}_2\text{P}/\text{Co}_2\text{P}_2\text{O}_7$  crystal phases. Hence, the crystalline phosphate and phosphide structures

within the composition do not change upon Ir decoration of the crystalline surfaces (Fig. 2c–d). Fig. 2c–d show relatively fine aggregated polycrystalline heterostructured materials at the interface of  $\text{Co}_2\text{P}/\text{Co}_2\text{P}_2\text{O}_7$ . The heterojunction interface with both phases should provide more accessible crystal defects and active sites, which is favorable for enhancing kinetics and enhancing the electrocatalytic activity. Furthermore, the HAADF-STEM image in Fig. 2e displays two distinct regions: bright and dark areas representing phases A and B, respectively, which are attributed to the behavior of the signal selection interface and the NP overlap of the heterostructure. Furthermore, The elemental distribution of the  $\text{Ir}_{0.05}\text{-Co}_2\text{P}/\text{Co}_2\text{P}_2\text{O}_7$  heterostructure was characterized using STEM-EDS mapping, as shown in Fig. 2f (inset image of Ir-containing phosphide/phosphate). The distributions of Co (green), P (blue), O (pink), and Ir (red color) are shown in Fig. 2g–j, respectively. Furthermore, STEM-EDS color mapping confirms that phase A contains only heavier Co, P, and Ir atoms and phase B contains Co, P, Ir, and O, which respectively represent Ir- $\text{Co}_2\text{P}$  and the phosphate phase, Ir- $\text{Co}_2\text{P}_2\text{O}_7$ , of the heterostructure. The contrast in the crystalline regions were used to assess the distribution of Ir atoms on the crystalline phosphide/phosphate based on the number of Ir relative to Co, P, and O. The imaging of the sample using HAADF/HAADF-STEM, as shown in

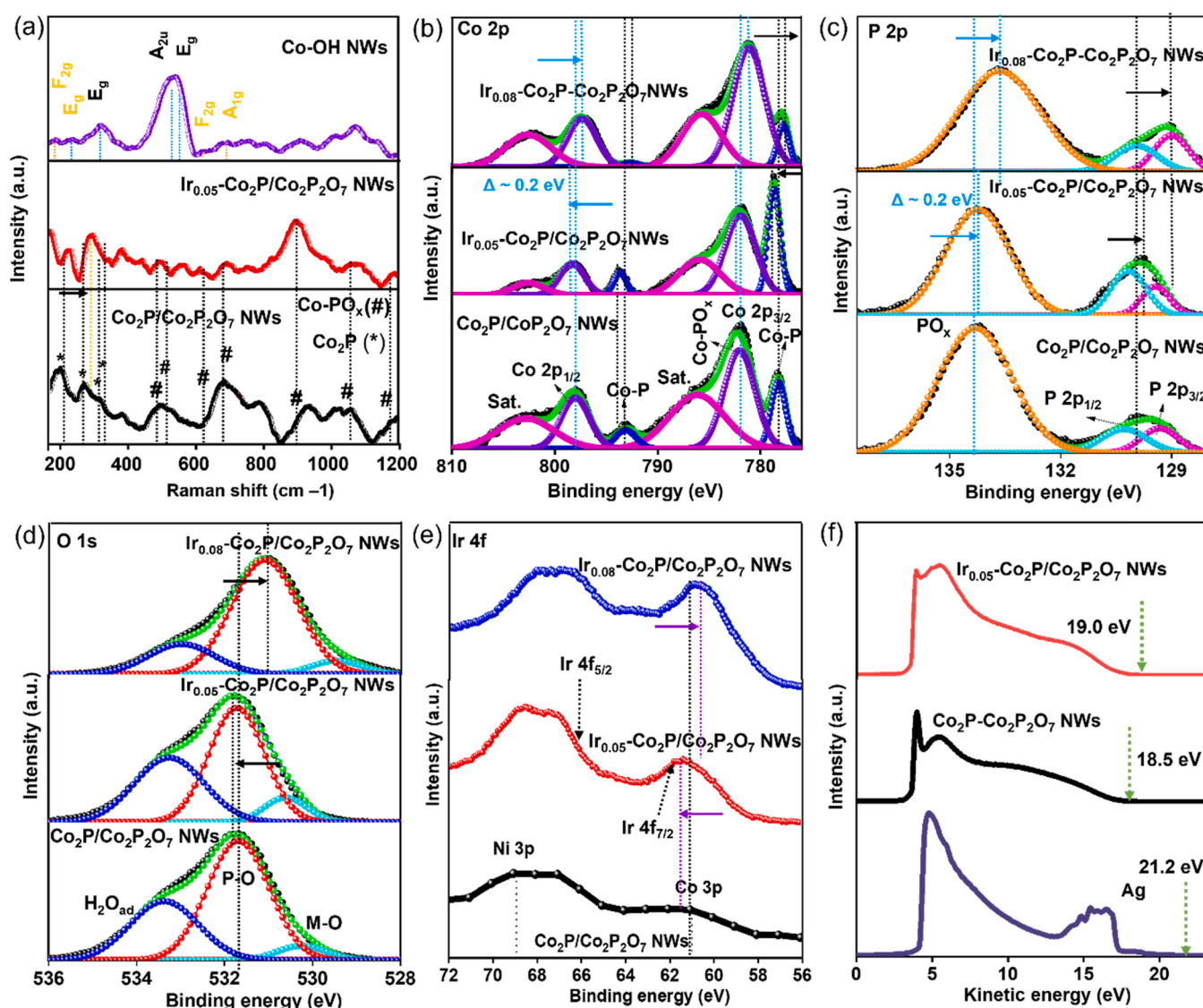


Fig. 3. (a) Raman spectra of the Co-OH nanowires (NWs),  $\text{Co}_2\text{P}/\text{Co}_2\text{P}_2\text{O}_7$  NWs, and  $\text{Ir}_{0.05}\text{-Co}_2\text{P}/\text{Co}_2\text{P}_2\text{O}_7$  NWs, (b) Co 2p, (c) P 2p, (d) O 1s, and (e) Ir 4f X-ray photoelectron and (f) ultraviolet photoelectron spectra of the  $\text{Co}_2\text{P}/\text{Co}_2\text{P}_2\text{O}_7$  NWs and  $\text{Ir}_{0.05}\text{-Co}_2\text{P}/\text{Co}_2\text{P}_2\text{O}_7$  NWs.

Fig. 2k–m, reveals many bright dots, which represent the Ir atoms over the entire heterostructure, with particles with sizes of 0.25–1 nm shown in Figs. S7a–b. The estimated average Ir diameter is 0.3 nm, as shown in Fig. S7b, indicating the successful formation of Ir clusters. The increase in particle diameter with increasing soaking concentrations from 0.05 to 1.0 mM  $\text{IrCl}_3 \cdot x\text{H}_2\text{O}$  is also shown in Fig. S8.

$\text{Ir}_{0.05}\text{-Co}_2\text{P/Co}_2\text{P}_2\text{O}_7$ , with a hierarchical structure and uniform dispersion, ameliorates the catalytic activity and is thus a powerful catalyst. The Raman spectra reveal the structures of the Co-OH NWs, as shown in Fig. 3a, with peak positions corresponding to  $\text{Co}_3\text{O}_4$  and Co-OH [46]. In addition, new peaks corresponding to  $\text{Co}_2\text{P}$  (230, 280, 295, and  $320\text{ cm}^{-1}$ ) are detected in the typical Raman spectrum of the  $\text{Co}_2\text{P/Co}_2\text{P}_2\text{O}_7$  NWs [42]. Furthermore, the weak peak at  $1033\text{ cm}^{-1}$  is assigned to  $\text{PO}_3$ , and the peaks at 236, 327, 379, 484, 513, 625, 754, 889, and  $1099\text{ cm}^{-1}$  correspond to the P–O–P in  $\text{Co}_2\text{P}_2\text{O}_7$ , indicating the formation of cobalt phosphate [47]. The shifts of the bands in the Raman spectrum of the  $\text{Ir}_{0.05}\text{-Co}_2\text{P/Co}_2\text{P}_2\text{O}_7$  NWs compared to those observed in the spectrum of the pure  $\text{Co}_2\text{P/Co}_2\text{P}_2\text{O}_7$  NWs reveal the Ir interact on the crystalline surface. The atomic Ir dopants are located on the  $\text{Co}_2\text{P/Co}_2\text{P}_2\text{O}_7$  phase. The elemental compositions and bonding states of all catalyst materials were investigated using XPS, as shown in Figs. S9 and S10a, revealing the presence of Ir, Co, O, and P, which agrees with EDS mapping results. As presented in Fig. S11a–b, the high-resolution Co 2p spectra of the Co-OH NWs exhibits typical Co  $2p_{1/2}$  and Co  $2p_{3/2}$  peaks, with adjacent satellite peaks, denoting the coexistence of  $\text{Co}^{2+}$  (797.5 and 781.9 eV) and  $\text{Co}^{3+}$  (795.6 and 780.0 eV) [48]. Furthermore, the spectra of the resulting  $\text{Co}_2\text{P/Co}_2\text{P}_2\text{O}_7$  NWs exhibit peaks at 778.3 eV, which are associated with Co  $2p_{3/2}$  and shift to a higher binding energy than that of Co metal [38]. This indicates the presence of Co with a partial positive charge of 1.5 eV ( $\text{Co}^+$ ) in the Co-P phase. Additionally, two satellite peaks representing Co  $2p_{3/2}$  and Co  $2p_{1/2}$  are detected at 786.4 and 803.0 eV, respectively (Fig. S11b) [48]. Peaks at 782.0 (Co  $2p_{3/2}$ ), 797.9 (Co  $2p_{1/2}$ ), and 134 eV are all attributed to oxidized Co and P of cobalt phosphate, and the P 2p binding energy of 129.2 eV differs significantly from that of elemental P (Fig. 3b–c and S11c) [49]. Based on the determined binding energies of the  $\text{Co}_2\text{P/Co}_2\text{P}_2\text{O}_7$  NWs, P exhibits a partial negative charge, whereas Co within Co-P exhibits a partial positive charge, indicating charge transfer from Co to P [50]. The analysis results of TEM, XRD, Raman spectroscopy, and XPS verify that the existence of the dual phosphide/phosphate structures in the resulting material should favor the electronic interactions between  $\text{Co}_2\text{P/Co}_2\text{P}_2\text{O}_7$ , thereby enhancing the interfacial reactivity in catalysis. Compared to those in the spectrum of the  $\text{Ir}_{0.05}\text{-Co}_2\text{P/Co}_2\text{P}_2\text{O}_7$  NW material, the peaks representing Co-P and Co- $\text{PO}_x$  in the XPS Co 2p spectra of the  $\text{Ir}_{0.05}\text{-Co}_2\text{P/Co}_2\text{P}_2\text{O}_7$  NWs exhibit positive shifts of 0.2 eV and negative peak shift of P 2p (Fig. 3b–c). This indicates potential electron transfer from Ir to P [51]. When Ir is present at 0.08 wt%, the peaks representing Co  $2p_{1/2}$  and Co  $2p_{3/2}$  are negatively shifted by 0.3 eV compared to those in the spectrum of the  $\text{Co}_2\text{P/Co}_2\text{P}_2\text{O}_7$  NW material (Fig. 3b). As presented in Fig. 3c, the negative shift of the peak representing  $\text{PO}_x$  is assigned to oxidized P ( $\text{PO}_3^{4-}$ ) within the material reducing, which is formed via the increasing Ir exposure [27,52,53]. As shown in Fig. 3d and S11d, the high-resolution O 1s spectra of all materials are deconvoluted into three peaks which agree with metal-O (O-Co in metal- $\text{PO}_x$ ), P-O(in  $\text{PO}_x$ ), and O-H in adsorbed  $\text{H}_2\text{O}$ , respectively [49]. Peak O1s decreased and negative left shifts as Ir increased to 0.08 wt% Ir. It could imply that incorporating metal species can reduce the oxidized degree of Co ions in the air. The positive peaks of O1s in  $\text{Ir}_{0.05}\text{-Co}_2\text{P/Co}_2\text{P}_2\text{O}_7$  NWs indicate that Ir binds to O and causes the peak to shift with electron transfer. Fig. 3e and S12 show that the peaks in the high-resolution Ir 3d and Ir 4f spectra of the  $\text{Ir}_{0.05}\text{-Co}_2\text{P/Co}_2\text{P}_2\text{O}_7$  NWs are clearly positively shifted by about 0.2 eV. On the other hand, these peaks have a 0.2 eV negative shift in the spectra of the  $\text{Ir}_{0.08}\text{-Co}_2\text{P/Co}_2\text{P}_2\text{O}_7$  NWs. Furthermore, the strong interactions between Ir and  $\text{Co}_2\text{P/Co}_2\text{P}_2\text{O}_7$  are revealed by the shifts in the binding energies of the

Co, O, Ir, and P peaks [37,54]. The Ir 4f, and Co 2p spectra of the  $\text{Ir}_{0.05}\text{-Co}_2\text{P/Co}_2\text{P}_2\text{O}_7$  NWs exhibit positive peak shifts, which indicate favorable electron transfer from Co and Ir to P of  $\text{Co}_2\text{P/Co}_2\text{P}_2\text{O}_7$  at the heterointerface, providing abundant active sites for electrochemical reactions. Furthermore, as displayed in Fig. 3f, the work function of the  $\text{Ir}_{0.05}\text{-Co}_2\text{P/Co}_2\text{P}_2\text{O}_7$  NW material (2.2 eV) is smaller than that of the  $\text{Co}_2\text{P/Co}_2\text{P}_2\text{O}_7$  NW material (2.7 eV), indicating electron transfer and a resultant increase in the Fermi level. The increased Fermi level energy of the catalyst surface may promote charge transfer to adsorbates and enhance chemical adsorption [55]. Relating the electric properties to the chemical activity is critical in determining the size effect on catalysis. However, it may prevent the blocking of numerous catalytic sites, thereby improving the HER/OER performances, and thus, the electronic and structural properties of the heterostructured  $\text{Ir}_{0.05}\text{-Co}_2\text{P/Co}_2\text{P}_2\text{O}_7$  material were predicted using density functional theory (DFT) analysis. The models of the materials are shown in Fig. 4a, which displays the top and side views of all samples. As observed in the experimental studies, the lattice structures of  $\text{Co}_2\text{P}$  and  $\text{Co}_2\text{P}_2\text{O}_7$  are optimized with the 112 and 120 planes, respectively.

To replicate the experimental results, the heterojunction material is optimized with and without the Ir cluster, and the size of the Ir cluster is  $\sim 1$  nm. Fig. 4a shows the Ir clusters adsorbed on the heterostructured  $\text{Co}_2\text{P/Co}_2\text{P}_2\text{O}_7$  material. Density of states (DOS) calculations for  $\text{Co}_2\text{P}$ ,  $\text{Co}_2\text{P}_2\text{O}_7$ ,  $\text{Co}_2\text{P/Co}_2\text{P}_2\text{O}_7$ , and the Ir clusters on  $\text{Co}_2\text{P/Co}_2\text{P}_2\text{O}_7$  are shown in Fig. 4b. Compared to those of  $\text{Co}_2\text{P}$  and  $\text{Co}_2\text{P}_2\text{O}_7$ , the  $\text{Co}_2\text{P/Co}_2\text{P}_2\text{O}_7$  lattice displays an increased Fermi population. DOS was analyzed to determine the source of rapid charge transfer and the capacity of the layer of Ir on  $\text{Co}_2\text{P/Co}_2\text{P}_2\text{O}_7$  to bind to intermediates. The DOS of  $\text{Ir-Co}_2\text{P/Co}_2\text{P}_2\text{O}_7$  reveals the dominance of the electronic states around the Fermi level, which is superior to those of  $\text{Co}_2\text{P/Co}_2\text{P}_2\text{O}_7$ ,  $\text{Co}_2\text{P}_2\text{O}_7$ , and  $\text{Co}_2\text{P}$ . This suggests that this material exhibits an enhanced binding potential and electron transfer to enhance the catalytic activity. Furthermore, the interconnected Ir on the  $\text{Co}_2\text{P/Co}_2\text{P}_2\text{O}_7$  lattice exhibits a significantly increased population around the Fermi level (in spin-up) in the DOS (Fig. 4b), indicating an Ir doping-induced increase in the population around the Fermi level. The d-orbital-projected DOSs of the Ir atoms in the Ir cluster on the  $\text{Co}_2\text{P/Co}_2\text{P}_2\text{O}_7$  lattice and the projected d-orbital populations of the Co atoms show that a significant proportion of the  $d_{xz}$ ,  $d_{yz}$ , and  $d_{xy}$  populations in the frontier orbitals may interact more strongly with the adsorbates in electrocatalytic OERs. This results in good active sites for water-splitting reactions (Fig. 4c–d and S13).  $\Delta G_{\text{H}^*}$  was used as a significant theoretical indicator in predicting the HER activity of the material. A  $\Delta G_{\text{H}^*}$  of almost 0 eV may provide a suitable HER activity, with a low reaction barrier and feasible desorption of generated hydrogen, for an optimal electrocatalyst, and the  $\Delta G_{\text{H}^*}$  of approximately 0 eV is generally required for an ideal HER electrocatalyst. Furthermore, pure  $\text{Co}_2\text{P}$ , which displays more HER active sites (Fig. 4e) than those on  $\text{Co}_2\text{P}_2\text{O}_7$ , exhibits high  $\Delta G_{\text{H}^*}$  values of  $-0.883$  and  $-2.624$  eV for the P and Co sites, respectively. The magnitudes of the  $\Delta G_{\text{H}^*}$  values of  $\text{Co}_2\text{P/Co}_2\text{P}_2\text{O}_7$  are significantly reduced to 0.169 and  $-0.372$  eV at the P and Co sites of  $\text{Co}_2\text{P}$ , respectively, and  $-0.395$  and 0.5195 eV at these respective sites in the  $\text{Co}_2\text{P}_2\text{O}_7$  hetero-lattice (Fig. 4f). Furthermore, the HER performance of the Ir-doped  $\text{Co}_2\text{P/Co}_2\text{P}_2\text{O}_7$  lattice is improved, with a significant increase in the HER activity. The  $\Delta G_{\text{H}^*}$  on P ( $-0.148$  eV) is almost 0 eV (Fig. 4g), and thus, the  $\Delta G_{\text{H}^*}$  values at the P centers in  $\text{Ir-Co}_2\text{P/Co}_2\text{P}_2\text{O}_7$  are superior to those at the P centers in  $\text{Co}_2\text{P}$ ,  $\text{Co}_2\text{P}_2\text{O}_7$ , and  $\text{Co}_2\text{P/Co}_2\text{P}_2\text{O}_7$ . The evaluated  $\Delta G_{\text{H}^*}$  values of these models agree with the experimental results. Hence, the atomic heterointerface engineering of  $\text{Co}_2\text{P/Co}_2\text{P}_2\text{O}_7$  may yield a rich interface that favors electron transfer and reconstitution of active sites, thus drastically enhancing the catalytic activity of the material. In addition, the OER performances of the Ir clusters on the hybrids in alkaline media are improved. The enhanced electrical conductivity of the phase may be attributed to the unique assembly of the  $\text{Ir-Co}_2\text{P/Co}_2\text{P}_2\text{O}_7$  NWs on the NF with an excellent conductivity and a large surface area. This yields abundant active sites and enables efficient mass



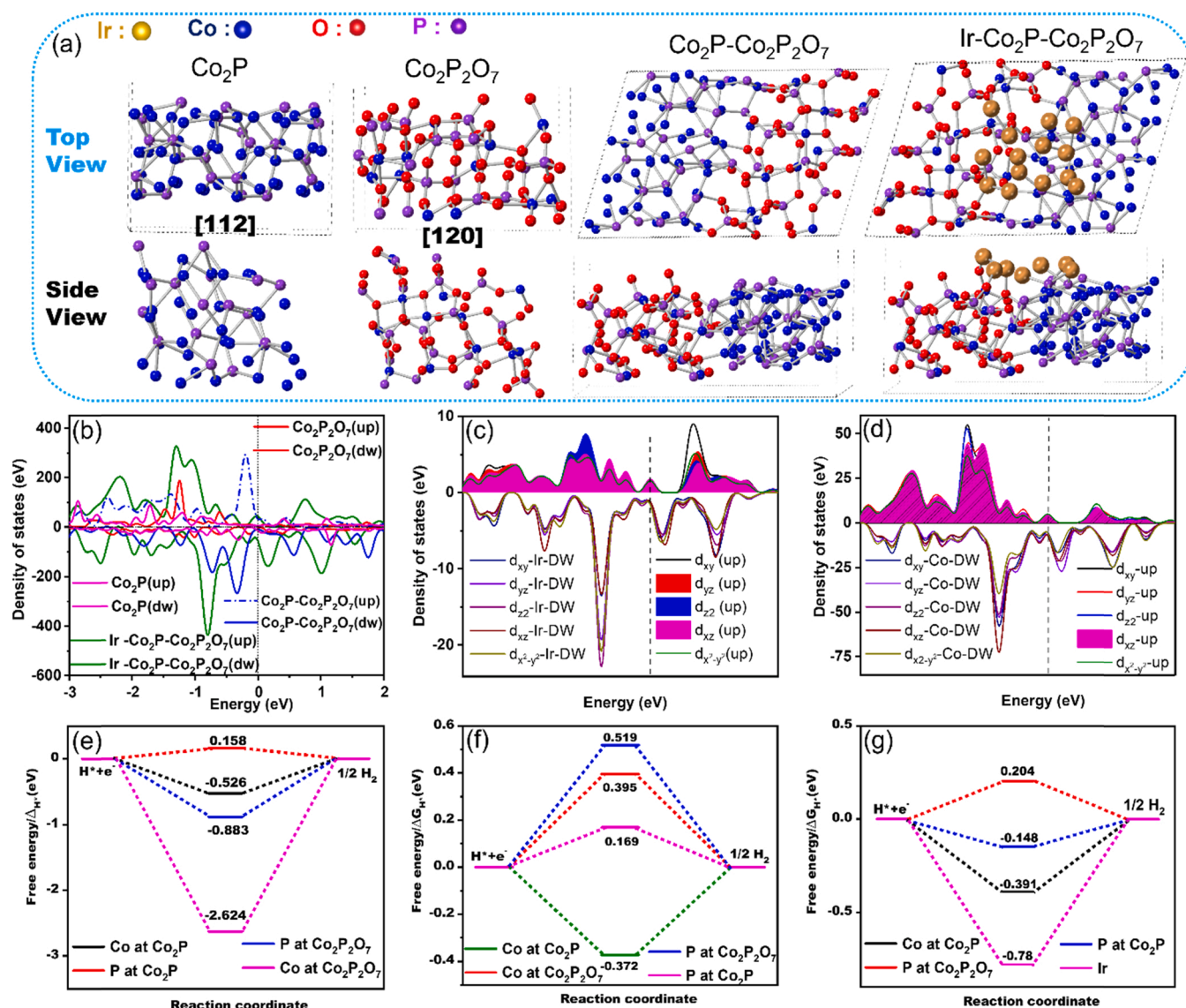


Fig. 4. (a) Schematic diagram of the atomic structures of the  $\text{Co}_2\text{P}$ ,  $\text{Co}_2\text{P}_2\text{O}_7$ ,  $\text{Co}_2\text{P}/\text{Co}_2\text{P}_2\text{O}_7$ , and  $\text{Ir}-\text{Co}_2\text{P}/\text{Co}_2\text{P}_2\text{O}_7$  layers, with top and side views, (b) total densities of states of  $\text{Co}_2\text{P}$ ,  $\text{Co}_2\text{P}_2\text{O}_7$ ,  $\text{Co}_2\text{P}/\text{Co}_2\text{P}_2\text{O}_7$ , and  $\text{Ir}-\text{Co}_2\text{P}/\text{Co}_2\text{P}_2\text{O}_7$ , projected d orbitals of (c) Ir and (d) Co atoms, and hydrogen adsorption free energies of (e)  $\text{Co}_2\text{P}$  and  $\text{Co}_2\text{P}_2\text{O}_7$ , (f)  $\text{Co}_2\text{P}/\text{Co}_2\text{P}_2\text{O}_7$ , and (g)  $\text{Ir}-\text{Co}_2\text{P}/\text{Co}_2\text{P}_2\text{O}_7$ .

transfer and charge transfer.

### 3.2. Catalytic performances

Electrolytic hydrogen generation in SW without further treatment (including purification and desalination) may be beneficial in numerous coastal nations and islands, where freshwater is scarce [56]. However, the electrocatalytic HER in SW is challenging due to its highly corrosive nature and intrinsically low conductivity compared to that of 1.0 M KOH, resulting in activity and stability problems that affect most of the reported catalytic materials. Therefore, identifying an active, durable HER catalyst that may be used in a solution of mimic SW instead of simulated SW is critical (Table S2). At a potential scan rate of  $5 \text{ mV s}^{-1}$ , linear sweep voltammetry (LSV) was used to evaluate the HER performances of the catalytic materials in 1.0 M KOH, simulated, mimic, and natural SW. The effects of the Ir ratio on the optimal loading amount of  $\text{Ir}-\text{Co}_2\text{P}/\text{Co}_2\text{P}_2\text{O}_7$  NWs/NF were investigated. Fig. 5a and S14 show the IR-corrected polarization curves and those without correction, respectively, with  $\text{Ir}_{0.05}\text{-Co}_2\text{P}/\text{Co}_2\text{P}_2\text{O}_7$  NWs/NF exhibiting a lower overpotential ( $\eta$ ), more positive onset potential, and superior current

response in the HER in 1.0 M KOH compared to those of the  $\text{Ir}_{0.08}\text{-Co}_2\text{P}/\text{Co}_2\text{P}_2\text{O}_7$  NWs,  $\text{Ir}_{0.04}\text{-Co}_2\text{P}/\text{Co}_2\text{P}_2\text{O}_7$  NWs,  $\text{Co}_2\text{P}/\text{Co}_2\text{P}_2\text{O}_7$  NWs, and Co-OH NWs. The  $\text{Ir}_{0.05}\text{-Co}_2\text{P}/\text{Co}_2\text{P}_2\text{O}_7$  NWs require smaller values of 63 and  $98 \text{ mV cm}^{-2}$  at 10 and  $20 \text{ mA cm}^{-2}$ , respectively, compared to those required by the  $\text{Ir}_{0.08}\text{-Co}_2\text{P}/\text{Co}_2\text{P}_2\text{O}_7$  NWs (86 and  $108 \text{ mV cm}^{-2}$ ),  $\text{Ir}_{0.04}\text{-Co}_2\text{P}/\text{Co}_2\text{P}_2\text{O}_7$  NWs (101 and  $132 \text{ mV cm}^{-2}$ ),  $\text{Co}_2\text{P}/\text{Co}_2\text{P}_2\text{O}_7$  NWs (163 and  $219 \text{ mV cm}^{-2}$ ), and Co-OH NWs (185 and  $240 \text{ mV cm}^{-2}$ ). However, these values are larger than those required by commercial Pt-C (50 and  $62 \text{ mV cm}^{-2}$ ), as shown in Fig. S15.

Fig. S16 illustrates the HER kinetics of the various materials, revealing that the Tafel slope of  $\text{Ir}_{0.05}\text{-Co}_2\text{P}/\text{Co}_2\text{P}_2\text{O}_7$  NWs sample is approximately  $69 \text{ mV dec}^{-1}$ , which is higher than that of Pt/C ( $30 \text{ mV dec}^{-1}$ ) but significantly lower than those of the comparable samples of 84, 110, 163, and  $181 \text{ mV dec}^{-1}$ , respectively. This implies that the Volmer-Heyrovsky mechanism governs the accelerated reaction kinetics of the  $\text{Ir}_{0.05}\text{-Co}_2\text{P}/\text{Co}_2\text{P}_2\text{O}_7$  NW material in the HER in an alkaline medium [57]. The hydrogen-generation capacity of the  $\text{Ir}_{0.05}\text{-Co}_2\text{P}/\text{Co}_2\text{P}_2\text{O}_7$  NW material was then investigated in natural SW at pH 8.15, as shown in Figs. S17a–b, and simulated and mimic SW. LSV of  $\text{Ir}_{0.05}\text{-Co}_2\text{P}/\text{Co}_2\text{P}_2\text{O}_7$  NW in Fig. 5b shows step-by-step decreases in

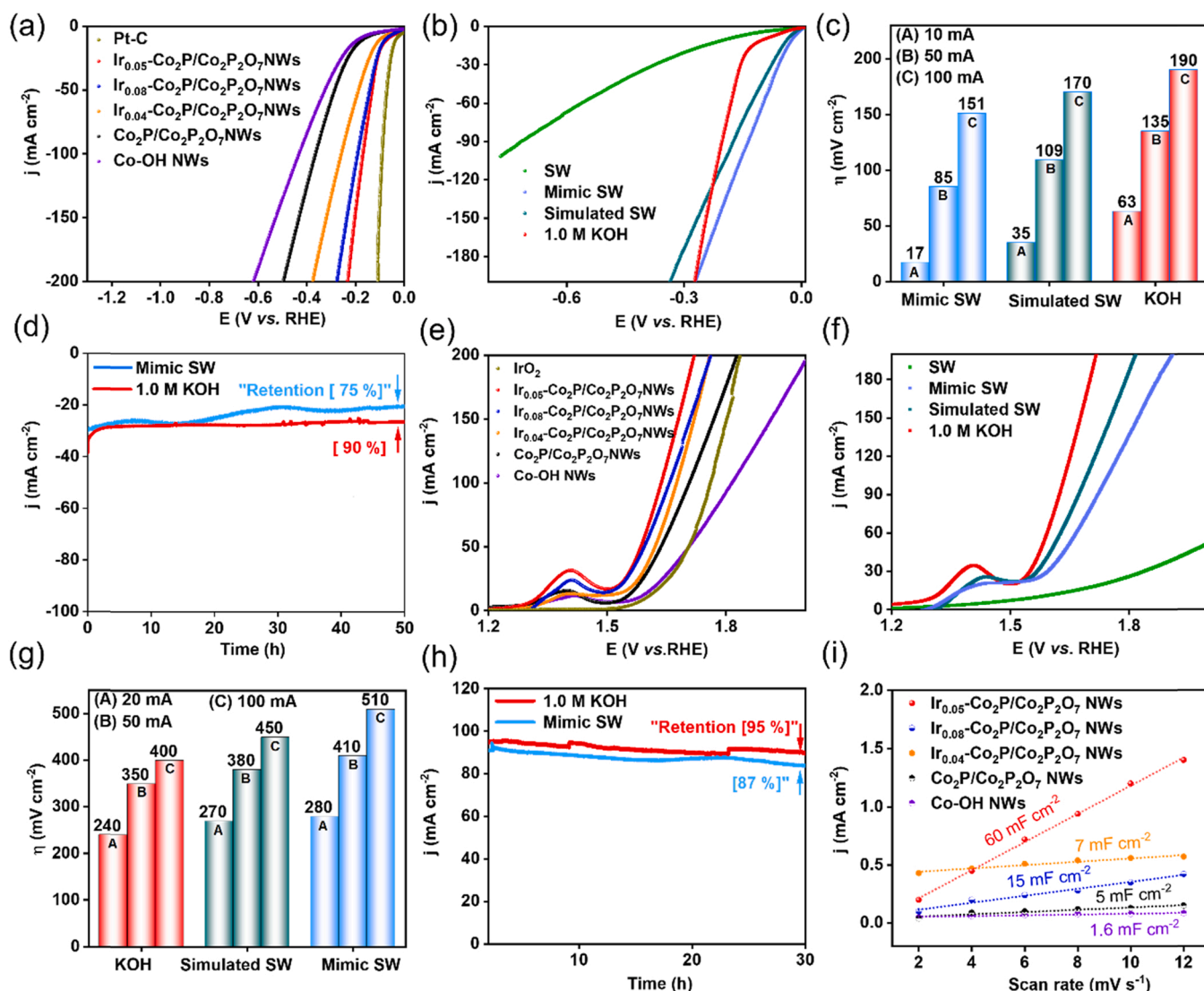


**Fig. 5.** (a) Hydrogen evolution reaction (HER) polarization curves of different materials, (b) linear sweep voltammetry (LSV) of HER for the  $\text{Ir}_{0.05}\text{-Co}_2\text{P/Co}_2\text{P}_2\text{O}_7$  nanowires (NWs), (c) overpotentials of HER of the  $\text{Ir}_{0.05}\text{-Co}_2\text{P/Co}_2\text{P}_2\text{O}_7$  NWs at 10, 50, and 100  $\text{mA cm}^{-2}$  in different electrolytes, (d) amperometric stabilities of the HER for the  $\text{Ir}_{0.05}\text{-Co}_2\text{P/Co}_2\text{P}_2\text{O}_7$  NWs in 1.0 M KOH and mimic seawater (SW), (e) LSV of different materials for use in the oxygen evolution reaction (OER) in 1.0 M KOH, (f) LSV of OER for the  $\text{Ir}_{0.05}\text{-Co}_2\text{P/Co}_2\text{P}_2\text{O}_7$  NWs in different environments, (g) overpotentials of OER of the  $\text{Ir}_{0.05}\text{-Co}_2\text{P/Co}_2\text{P}_2\text{O}_7$  NWs at 20, 50, and 100  $\text{mA cm}^{-2}$  in different electrolytes, (h) amperometric stabilities of the OER for the  $\text{Ir}_{0.05}\text{-Co}_2\text{P/Co}_2\text{P}_2\text{O}_7$  NWs in 1.0 M KOH and mimic SW, and (i) double-layer capacitances ( $C_{dl}$ ) of the different materials.

activity in mimic SW, simulated SW, natural SW, and 1.0 M KOH, respectively. This may be due to active site obstruction and conductivity degradation in the complex SW electrolytes, but the  $\text{Ir}_{0.05}\text{-Co}_2\text{P/Co}_2\text{P}_2\text{O}_7$  NW catalyst exhibits a high HER activity in mimic SW, as shown in Fig. 5c. To realize current densities of 10  $\text{mA cm}^{-2}$  in mimic SW, simulated SW, 1.0 M KOH, and natural SW potentials of 17, 35, 63, and 205 mV  $\text{cm}^{-2}$  are required. The  $\eta$  values of  $\text{Ir}_{0.05}\text{-Co}_2\text{P/Co}_2\text{P}_2\text{O}_7$  NWs/NF at 10  $\text{mA cm}^{-2}$  in mimic SW and natural SW and 1.0 M KOH are smaller than those reported previously (Tables S3 and S4). The Tafel slope of 30  $\text{mV dec}^{-1}$  of the  $\text{Ir}_{0.05}\text{-Co}_2\text{P/Co}_2\text{P}_2\text{O}_7$  NWs in mimic SW is much smaller than that in 1.0 M KOH (69  $\text{mV dec}^{-1}$ ) and similar to that in simulated SW (Fig. S18a). The Tafel slope of the  $\text{Ir}_{0.05}\text{-Co}_2\text{P/Co}_2\text{P}_2\text{O}_7$  NWs in mimic SW indicates that catalysis follows the Volmer-Heyrovsky pathway [49]. Under HER conditions, the cations in SW, such as Na, Ca, and Mg, may be deposited on the electrode surface [58], which blocks the catalytic sites, reduces the accessible surface area, and finally leads to catalyst deactivation. Therefore, an in-depth study of the stability of the electrode during the HER in alkaline SW splitting is required for the catalyst to be used in practice. Long-term stability tests of the

$\text{Ir}_{0.05}\text{-Co}_2\text{P/Co}_2\text{P}_2\text{O}_7$  NW catalyst were carried out for 50 h at a constant current density of  $-30 \text{ mA cm}^{-2}$  in 1.0 M KOH and mimic SW. The results, revealing maintenances of 90% and 75%, respectively, are displayed in Fig. 5d, corresponding to the LSV after the stability studies shown in Figs. S19a–b. After evaluation for 50 h, the superior stability in the HER in 1.0 M KOH compared to that in alkaline SW splitting is revealed by the potential fluctuation, which is just 9 mV in 1.0 M KOH and 25 mV in mimic SW [59]. Therefore, the  $\text{Ir}_{0.05}\text{-Co}_2\text{P/Co}_2\text{P}_2\text{O}_7$  NW catalysts are highly robust and active in the HER in mimic SW and 1.0 M KOH. The anions in SW include chloride, sulfate, bicarbonate, and fluoride, and these anions, particularly chlorides, generally limit the OER via the CLER [5]. We thus investigated the OER and its activity over various materials, as shown in Fig. 5e. The optimized  $\text{Ir}_{0.05}\text{-Co}_2\text{P/Co}_2\text{P}_2\text{O}_7$  NW sample has an outstanding OER activity in 1.0 M KOH, with an  $\eta$  of 240 mV at 20  $\text{mA cm}^{-2}$ , which is superior to those of  $\text{Ir}_{0.08}\text{-Co}_2\text{P/Co}_2\text{P}_2\text{O}_7$  NWs (290 mV), the  $\text{Ir}_{0.04}\text{-Co}_2\text{P/Co}_2\text{P}_2\text{O}_7$  NWs (330 mV) and Co-OH NWs (390 mV),  $\text{Co}_2\text{P/Co}_2\text{P}_2\text{O}_7$  NWs (350 mV), and  $\text{IrO}_2$  (390 mV, Fig. S20). Tafel slopes were obtained to provide insights into the OER kinetics of the catalysts, as presented in Fig. S21,



with the  $\text{Ir}_{0.05}\text{-Co}_2\text{P/Co}_2\text{P}_2\text{O}_7$  NWs displaying the smallest Tafel slope of  $138 \text{ mV dec}^{-1}$ . This value is much smaller than those of  $\text{IrO}_2$  ( $149 \text{ mV dec}^{-1}$ ) and the  $\text{Ir}_{0.08}\text{-Co}_2\text{P/Co}_2\text{P}_2\text{O}_7$  NWs ( $144 \text{ mV dec}^{-1}$ ),  $\text{Ir}_{0.04}\text{-Co}_2\text{P/Co}_2\text{P}_2\text{O}_7$  NWs ( $147 \text{ mV dec}^{-1}$ ),  $\text{Co}_2\text{P/Co}_2\text{P}_2\text{O}_7$  NWs ( $148 \text{ mV dec}^{-1}$ ), and Co-OH NWs ( $166 \text{ mV dec}^{-1}$ ), indicating rapid, favorable OER kinetics and a higher activity. As shown in Fig. 5f, the LSV of the  $\text{Ir}_{0.05}\text{-Co}_2\text{P/Co}_2\text{P}_2\text{O}_7$  NWs material in 1.0 M KOH is enhanced compared to those obtained in mimic, simulated, and natural SW. In this context, in 1.0 M KOH, simulated SW, and mimic SW, respective values of 240, 270, and 280 mV are required, as indicated in Fig. 5g, to obtain current densities of  $20 \text{ mA cm}^{-2}$ . The catalytic performance of  $\text{Ir}_{0.05}\text{-Co}_2\text{P/Co}_2\text{P}_2\text{O}_7$  NWs in 1.0 M KOH is significantly superior to those of previously reported catalysts (Table S5). Additionally, in different environments, the catalyst exhibits various Tafel slopes due to the synergistic effects brought about by its distinctive structure. As shown in Fig. S18b, the Tafel slope of  $\text{Ir}_{0.05}\text{-Co}_2\text{P/Co}_2\text{P}_2\text{O}_7$  NWs in mimic SW is  $230 \text{ mV dec}^{-1}$ , which is higher than those in 1.0 M KOH ( $40 \text{ mV dec}^{-1}$ ) and simulated SW ( $92 \text{ mV dec}^{-1}$ ). As displayed in Table S5, the superior OER activity of  $\text{Ir}_{0.05}\text{-Co}_2\text{P/Co}_2\text{P}_2\text{O}_7$  NWs surpasses those of numerous electrocatalysts, further demonstrating its excellent intrinsic properties for expediting the OER in alkaline SW. We investigated the stabilities of  $\text{Ir}_{0.05}\text{-Co}_2\text{P/Co}_2\text{P}_2\text{O}_7$  NW samples in long-term OER operations in mimic SW and 1.0 M KOH. The catalyst exhibits good current response with 95% retention after 30 h in 1.0 M KOH, in contrast to an 87% retention in mimic SW (Fig. 5h). This corresponds to the LSV after the stability studies, as shown in Figs. S19c–d, with potential fluctuations of just 18 mV in 1.0 M KOH and 28 mV in mimic SW. The insoluble precipitates  $\text{Mg(OH)}_2$  and  $\text{Ca(OH)}_2$  coating the electrode surface and obstructing a few surface catalytic sites may be responsible for the slight decrease in activity [58]. The enhanced electroactive sites and exceptional charge transfer capacity of the  $\text{Ir}_{0.05}\text{-Co}_2\text{P/Co}_2\text{P}_2\text{O}_7$  NWs should account for their excellent catalytic performances in the HER and OER in 1.0 M KOH and mimic SW. These are caused by cooperative effects derived from the formation of the unique Ir nanoclusters on the 1D  $\text{Co}_2\text{P/Co}_2\text{P}_2\text{O}_7$  NW heterostructure. The electrochemical active surface areas (ECSAs) of the synthesized catalysts were then determined. All materials were subjected to cyclic voltammetry in 1.0 M KOH at potential scan rates of 2, 4, 6, 8, 10 and  $12 \text{ mV s}^{-1}$ , and the results are shown in Fig. 5i and S22. The double-layer capacitance (Cdl) of the  $\text{Ir}_{0.05}\text{-Co}_2\text{P/Co}_2\text{P}_2\text{O}_7$  NW sample is  $60 \text{ mF cm}^{-2}$ , which is dramatically higher than those of the  $\text{Ir}_{0.08}\text{-Co}_2\text{P/Co}_2\text{P}_2\text{O}_7$  NWs ( $15 \text{ mF cm}^{-2}$ ),  $\text{Ir}_{0.04}\text{-Co}_2\text{P/Co}_2\text{P}_2\text{O}_7$  NWs ( $7 \text{ mF cm}^{-2}$ ),  $\text{Co}_2\text{P/Co}_2\text{P}_2\text{O}_7$  NWs ( $5 \text{ mF cm}^{-2}$ ), Co-OH NWs ( $1.6 \text{ mF cm}^{-2}$ ), and NF ( $0.4 \text{ mF cm}^{-2}$ ), as shown in Fig. S23. The  $\text{Ir}_{0.05}\text{-Co}_2\text{P/Co}_2\text{P}_2\text{O}_7$  NWs,  $\text{Ir}_{0.08}\text{-Co}_2\text{P/Co}_2\text{P}_2\text{O}_7$  NWs,  $\text{Ir}_{0.04}\text{-Co}_2\text{P/Co}_2\text{P}_2\text{O}_7$  NWs,  $\text{Co}_2\text{P/Co}_2\text{P}_2\text{O}_7$  NWs, and Co-OH NWs display ECSAs of 150, 37.5, 17.5, 12.5, and  $3 \text{ cm}^2$ , respectively. The current density normalized by the ECSA reveals the intrinsic activity of the electrode, and Figs. S24a and S24b show that the  $\text{Ir}_{0.05}\text{-Co}_2\text{P/Co}_2\text{P}_2\text{O}_7$  NWs have higher catalytic activities in the OER and HER, respectively. The observed non-Faradaic potential region was used to further investigate the electrochemical properties of the  $\text{Ir}_{0.05}\text{-Co}_2\text{P/Co}_2\text{P}_2\text{O}_7$  NWs in different environments for application in water splitting. The Cdl values of the material in natural SW ( $11 \text{ mF cm}^{-2}$ ), simulated SW ( $33 \text{ mF cm}^{-2}$ ), and mimic SW ( $41 \text{ mF cm}^{-2}$ ) and 1.0 M KOH were calculated (Figs. S25a–d). These calculations were conducted in a manner that was highly correlated with the ECSAs of 27.5, 82.5, 102.5, and  $150 \text{ cm}^2$ , as shown in Fig. S26. The material exhibits the highest surface area of the materials studied in 1.0 M KOH. The  $\text{Ir}_{0.05}\text{-Co}_2\text{P/Co}_2\text{P}_2\text{O}_7$  NW material has excellent electrical properties, which are also confirmed by electrochemical impedance spectroscopy (EIS). An equivalent circuit made up of series resistance (Rs) and charge transfer resistance (Rct) and a capacitance (CPE), where Rct stands for the resistance between the catalyst and Ni substrate, and Rs for the resistance between the catalyst and electrolyte, is used to fit the EIS data (Fig. S27 and Table S6). The Nyquist plot of the  $\text{Ir}_{0.05}\text{-Co}_2\text{P/Co}_2\text{P}_2\text{O}_7$  NW material exhibits a semicircle with a smaller diameter compared to those in the Nyquist plots of the other samples. The Rct of

the  $\text{Ir}_{0.05}\text{-Co}_2\text{P/Co}_2\text{P}_2\text{O}_7$  NW material is only  $0.2 \Omega$ , which is drastically smaller than those of the  $\text{Ir}_{0.08}\text{-Co}_2\text{P/Co}_2\text{P}_2\text{O}_7$  NWs ( $0.3 \Omega$ ),  $\text{Ir}_{0.04}\text{-Co}_2\text{P/Co}_2\text{P}_2\text{O}_7$  NWs ( $0.48 \Omega$ ),  $\text{Co}_2\text{P/Co}_2\text{P}_2\text{O}_7$  NWs ( $0.5 \Omega$ ), and Co-OH NWs ( $1.48 \Omega$ ). The Rct of the  $\text{Ir}_{0.05}\text{-Co}_2\text{P/Co}_2\text{P}_2\text{O}_7$  NW material indicates its superior interfacial charge transfer and enhanced diffusion processes during catalytic reactions. Furthermore, the lateral heterostructures are formed with the interchange of highly conductive phosphide/phosphate phases to have a continuous junction with the optimized electronic structures of Ir atoms. This, coupled with the nanostructures formed by the Ir atoms, generates a higher number and type of catalytic sites, and highly favors fast hetero-charge transfer during catalysis. Therefore, the  $\text{Ir}_{0.05}\text{-Co}_2\text{P/Co}_2\text{P}_2\text{O}_7$  NW nano-support exhibits high conductivity and a large surface area and increases the exposed catalytic sites in the outer-shell nanocluster layer and accelerates charge transfer during the catalytic reaction. The electrolyzer with the optimized  $0.05 \text{ mM IrCl}_3 \cdot x\text{H}_2\text{O}$  ( $\text{Ir}_{0.05}\text{-Co}_2\text{P/Co}_2\text{P}_2\text{O}_7$  NW) sample exhibits excellent catalytic activity at 1.52 and 1.88 V to generate 10 and  $90 \text{ mA cm}^{-2}$  in 1.0 M KOH, with smaller cell voltages than those of the devices with the 0.1 mM (1.52 and 1.92 V), 1.0 mM (1.56 and 1.94 V), or 0.01 mM (1.63 and 1.98 V), respectively (Fig. S28).

The result indicates the effect of an Ir source with an optimized concentration on electrochemical performance and scientific value. A current output of  $10 \text{ mA cm}^{-2}$  is achieved with these devices using small potentials of 1.52, 1.60, 1.62, and 1.67 V in 1.0 M KOH, mimic, simulated, and natural SW, respectively, as presented in Fig. 6a. The LSV of the electrolyzer with  $\text{Ir}_{0.05}\text{-Co}_2\text{P/Co}_2\text{P}_2\text{O}_7$  NWs has a significant slope with a voltage at 1.52, 1.68 V, which is lower than that of  $\text{IrO}_2/\text{Pt-C}$  (1.58 V and 1.71 V at 10, and  $30 \text{ mA cm}^{-2}$ , respectively). This is demonstrated in Figs. S29a, indicating that its performances are superior to those of  $\text{IrO}_2/\text{Pt-C}$ . Furthermore, the  $\text{RuO}_2/\text{Pt-C}$  devices require a lower voltage at  $30 \text{ mA cm}^{-2}$  in 1.0 M KOH (1.62 V), mimic (1.61 V), and simulated SW (1.62 V) than the  $\text{Ir}_{0.05}\text{-Co}_2\text{P/Co}_2\text{P}_2\text{O}_7$  NWs electrolyzer (Fig. S29a–c). However, the electrolyzer with  $\text{Ir}_{0.05}\text{-Co}_2\text{P/Co}_2\text{P}_2\text{O}_7$  NWs in natural SW outperforms the  $\text{RuO}_2/\text{Pt-C}$  electrolyzer. It requires 1.97 V to achieve a current output of  $30 \text{ mA cm}^{-2}$  in SW, which is 0.35 V less than the  $\text{RuO}_2/\text{Pt-C}$  electrolyzer (Fig. S29d). The respective cell potentials of 1.60 and 1.67 V in mimic and natural SW, respectively, are far superior to the performances of various previously reported catalytic systems in these environments (Table S7). Remarkably, in SW and alkaline electrolytes, the electrolyzer with the  $\text{Ir}_{0.05}\text{-Co}_2\text{P/Co}_2\text{P}_2\text{O}_7$  NWs shows outstanding overall SW splitting performance. As shown in Fig. 6b, at  $25^\circ\text{C}$ , the cell potential required to obtain a current density of  $10 \text{ mA cm}^{-2}$  is 1.53 V in mimic SW containing 5.0 M KOH electrolytes. The performances of these  $\text{Ir}_{0.05}\text{-Co}_2\text{P/Co}_2\text{P}_2\text{O}_7$ -based devices were calculated at various working temperatures, as shown in Fig. 6c, to further investigate their practical applications. The cell potentials are further decreased to 1.62, 1.48, and 1.45 V at a current density of  $20 \text{ mA cm}^{-2}$  in a solution mimic containing 5.0 M KOH electrolytes by heating the electrolyte to 25, 45, or  $60^\circ\text{C}$ , respectively. The application can be used by simply increasing the working temperature with a solar hot water system [60]. These developed devices have superior catalytic performance in mimic SW to those observed in simulated and natural SW. This may be a result of the excellent charge transfer capacity of the electrode in the environment, in addition to the higher conductivity of the mimic SW electrolyte (Fig. 6d). The Faradaic efficiency of the electrolyzer in mimic SW at room temperature was then analyzed by gathering the gaseous products on the anode and cathode. Only  $\text{H}_2$  and  $\text{O}_2$  gases in molar ratios of almost 2:1 is detected, as shown in Fig. 6e, and the Faradaic efficiencies are approximately 94.2% (OER) and 96.5% (HER) during mimic SW electrolysis, indicating the high performances of the OER and HER at the electrodes. Furthermore, we proposed an integrated device comprising series-connected commercial solar cells and  $\text{Ir}_{0.05}\text{-Co}_2\text{P/Co}_2\text{P}_2\text{O}_7$  NW catalytic electrodes that may be immersed directly in an aqueous solution of mimic SW to be used for solar-driven water splitting in the Republic of Korea at  $27^\circ\text{C}$  under natural sunlight. The continuous release of  $\text{O}_2$  and  $\text{H}_2$  bubbles from both electrodes is

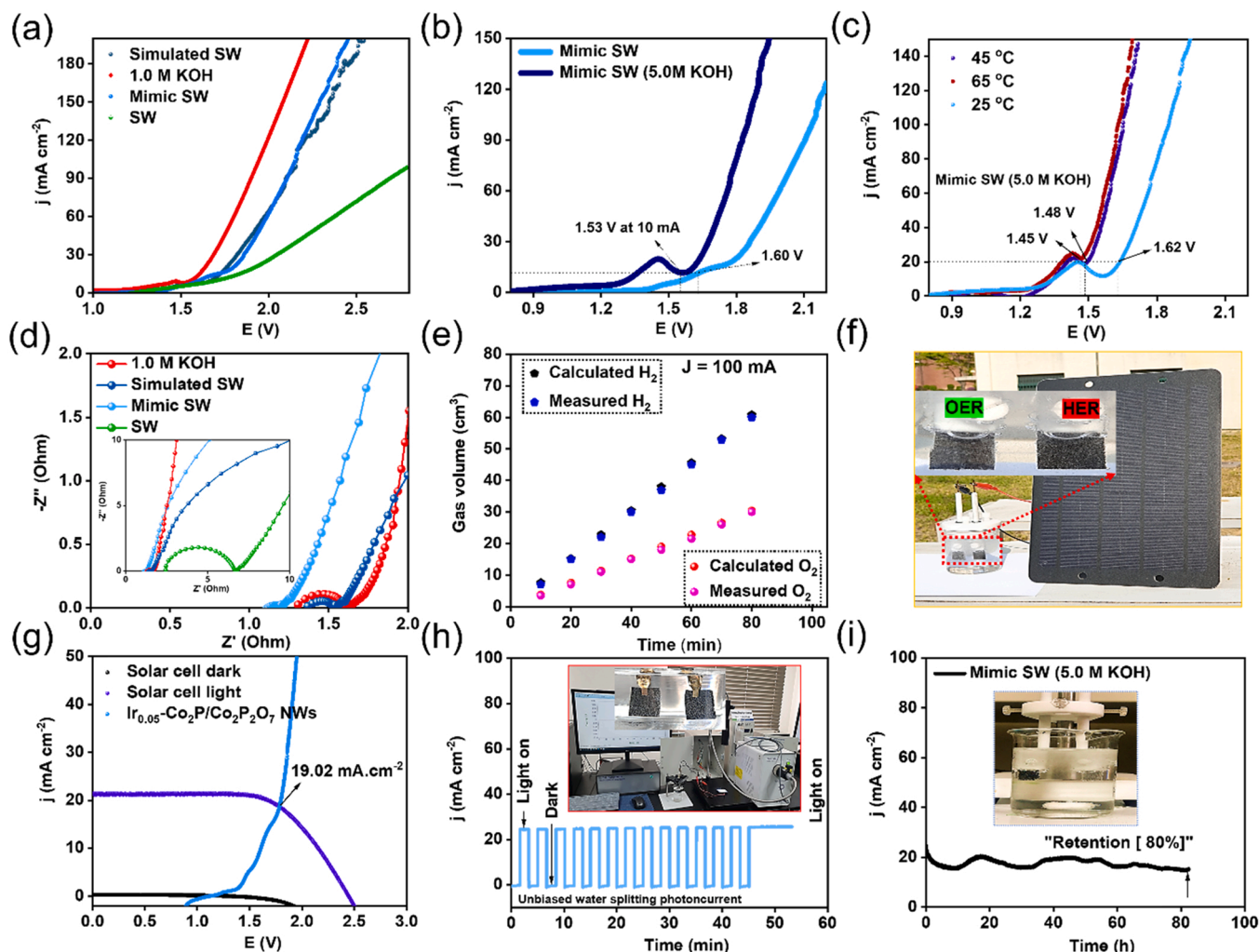


**Fig. 6.** (a) LSV of the overall water-splitting devices in 1.0 M KOH, mimic, simulated, and natural seawater (SW), (b) LSV showing the cell potentials of the  $\text{Ir}_{0.05}\text{-Co}_2\text{P/Co}_2\text{P}_2\text{O}_7$  nanowire (NW) materials in mimic SW at different alkaline concentrations, (c) electrolyzer performances of the  $\text{Ir}_{0.05}\text{-Co}_2\text{P/Co}_2\text{P}_2\text{O}_7$  NWs in 5.0 M KOH and SW at 25, 45, and 65 °C, (d) Nyquist plots of the  $\text{Ir}_{0.05}\text{-Co}_2\text{P/Co}_2\text{P}_2\text{O}_7$  NW catalysts in different environments, (e) Faradic efficiency of the device in mimic SW, (f) images of the device under natural sunlight in the Republic of Korea at 27 °C during mimic SW splitting, (g) current density-voltage (J-V) curves of a commercial silicon solar cell combined with an electrolyzer collected in darkness and under simulated AM 1.5 G 100 mW cm<sup>-2</sup> illumination, (h) time-resolved photoresponse of the incorporated device without external bias under chopped computer simulation solar light, and (i) durability study of the  $\text{Ir}_{0.05}\text{-Co}_2\text{P/Co}_2\text{P}_2\text{O}_7$  NW material at a constant current density in a mimic solution of 5.0 M KOH and SW.

observed when this photo-assisted mimic SW splitting device is operated in sunlight, demonstrating the successful production of  $\text{H}_2$  (Fig. 6f). Fig. 6g shows the current-potential curve of the commercial silicon solar cell. The solar-to-hydrogen (STH) efficiency estimated from the intersection of the polarization curve of the electrolyzer and the power curve of the solar cell yields an STH efficiency of 22.4% [61]. The commercial silicon solar cells were put alongside and associated via wires to the immersed catalytic electrodes, and the energy for water splitting was provided by simulated solar irradiation (inset in Fig. 6h). To confirm the operating current density, we used chopped simulated solar-light illumination to assess time-resolved photoresponse of the integrated device (Fig. 6h), yielding a value that closely matches that derived from Fig. 6g. Furthermore, operating durability is critical in assessing the performance of an electrolyzer and furthering its industrial applications. The electrolyzer may retain its outstanding overall alkaline SW splitting performance with a small degradation, displaying a retention of 92% over 40 h of operation at a stable current density of 20 mA cm<sup>-2</sup> in mimic SW (Fig. S30a). The performances of both electrodes of the  $\text{Ir}_{0.05}\text{-Co}_2\text{P/Co}_2\text{P}_2\text{O}_7$  NW device in mimic SW is the same as those in simulated SW and 1.0 M KOH electrolytes (Figs. S30b–c). Moreover, a commercial catalyst comprising  $\text{IrO}_2$  and Pt-C systems, as presented in

Fig. S30d, displays a lower activity and stability in mimic SW, with a retention 56% after 10 h, compared to those of the device based on the  $\text{Ir}_{0.05}\text{-Co}_2\text{P/Co}_2\text{P}_2\text{O}_7$  NWs. Furthermore, we investigated the stability of the catalyst in mimic SW containing 5.0 M KOH electrolytes (Fig. 6i). The catalyst displays an outstanding performance and stability at 20 mA cm<sup>-2</sup> after 80 h, with a retention of 80% in overall alkaline SW splitting. These results effectively demonstrate the good potential of the  $\text{Ir}_{0.05}\text{-Co}_2\text{P/Co}_2\text{P}_2\text{O}_7$  NW catalyst as an economic, active, stable candidate for use in practical electrolysis in alkaline 1.0 M KOH environments and mimic SW.

#### 4. Conclusions

We successfully synthesized and optimized novel Ir (0.05 wt%)-integrated phosphide/phosphate heterostructured NWs on NF as a free-standing electrode via impregnation and phosphidation, and this electrode exhibited excellent catalytic properties in overall water splitting. Ir deposition on the phosphide/phosphate catalytic substrate was also based on an atomic-level understanding of the dynamic structural transformation. The  $\text{Ir}_{0.05}\text{-Co}_2\text{P/Co}_2\text{P}_2\text{O}_7$  NW/NF bifunctional electrocatalyst was developed for use in overall water splitting, with cell



potentials at 10 mA cm<sup>-2</sup> of 1.52, 1.60, 1.62, and 1.67 V in 1.0 M KOH and mimic, simulated, and natural SW, respectively. Furthermore, the Ir<sub>0.05</sub>-Co<sub>2</sub>P/Co<sub>2</sub>P<sub>2</sub>O<sub>7</sub> NW/NF material displayed an excellent electrocatalytic performance in mimic SW and Faradic efficiencies of 96.5% and 94.2% in H<sub>2</sub> and O<sub>2</sub> evolution, respectively. The developed devices also exhibited catalytic performances in mimic SW at various working temperatures. Therefore, the photo-assisted mimic SW splitting system designed in this study could be used to produce hydrogen cost-effectively in SW while reducing the consumption of highly unfavorable freshwater. DFT analysis, which was used to explain the experimental results, elucidated the active sites of Ir-Co<sub>2</sub>P/Co<sub>2</sub>P<sub>2</sub>O<sub>7</sub> at P ( $\Delta G_{H^*}$  = 0.148 eV) in the HER. Hence, the Ir<sub>0.05</sub>-Co<sub>2</sub>P/Co<sub>2</sub>P<sub>2</sub>O<sub>7</sub> NW material exhibits an excellent performance as a bifunctional catalyst with a high economic efficiency in practical SW splitting.

## CRediT authorship contribution statement

**Van Hien Hoa:** Conceptualization, Methodology, Investigation, Formal analysis, Writing – original draft. **Muthu Austeria:** Data curation, Methodology, Investigation, Formal analysis, Writing. **Huyen Thi Dao:** Data curation, Methodology, Investigation, Formal analysis. **Mai Mai:** Data curation, Methodology, Investigation, Formal analysis. **Do Hwan Kim:** Supervision, Project administration, Explanation, Writing – review & editing.

## Declaration of Competing Interest

The authors declare that they have no known competing financial interests or personal relationships that could have appeared to influence the work reported in this paper.

## Data Availability

Data will be made available on request.

## Acknowledgments

This research was supported by the Regional Leading Research Center Program (2019R1A5A8080326) and the Basic Science Research Program (2021R1F1A1048758, 2022R1I1A1A01053248) through the National Research Foundation funded by the Ministry of Science, ICT, and Future Planning of the Republic of Korea. The calculations were supported by the supercomputing resources (KSC-2021-CRE-0413) of the National Supercomputing Center (Daejeon, Republic of Korea).

## Appendix A. Supporting information

Supplementary data associated with this article can be found in the online version at [doi:10.1016/j.apcatb.2023.122467](https://doi.org/10.1016/j.apcatb.2023.122467).

## References

- [1] F. Sun, J. Qin, Z. Wang, M. Yu, X. Wu, X. Sun, J. Qiu, Energy-saving hydrogen production by chlorine-free hybrid seawater splitting coupling hydrazine degradation, *Nat. Commun.* 12 (2021) 1–11, <https://doi.org/10.1038/s41467-021-24529-3>.
- [2] X. Tao, Y. Zhao, S. Wang, C. Li, R. Li, Recent advances and perspectives for solar-driven water splitting using particulate photocatalysts, *Chem. Soc. Rev.* (2022) 3561–3608, <https://doi.org/10.1039/d1cs01182k>.
- [3] P. Sun, Y. Zhou, H. Li, H. Zhang, L. Feng, Q. Cao, S. Liu, T. Wågberg, G. Hu, Round-the-clock bifunctional honeycomb-like nitrogen-doped carbon-decorated Co<sub>2</sub>P/Mo<sub>2</sub>C-heterojunction electrocatalyst for direct water splitting with 18.1% STH efficiency, *Appl. Catal. B Environ.* 310 (2022), 121354, <https://doi.org/10.1016/j.apcatb.2022.121354>.
- [4] W. Tong, M. Forster, F. Dionigi, S. Dresp, R. Sadeghi Erami, P. Strasser, A.J. Cowan, P. Farràs, Electrolysis of low-grade and saline surface water, *Nat. Energy* 5 (2020) 367–377, <https://doi.org/10.1038/s41560-020-0550-8>.
- [5] Y. Zhao, B. Jin, Y. Zheng, H. Jin, Y. Jiao, S.Z. Qiao, Charge state manipulation of cobalt selenide catalyst for overall seawater electrolysis, *Adv. Energy Mater.* 8 (2018) 1–9, <https://doi.org/10.1002/aenm.201801926>.
- [6] H. Zhang, A.W. Maijenburg, X. Li, S.L. Schweizer, R.B. Wehrspohn, Bifunctional heterostructured transition metal phosphides for efficient electrochemical water splitting, *Adv. Funct. Mater.* 30 (2020), <https://doi.org/10.1002/adfm.202003261>.
- [7] C.C.L. McCrory, S. Jung, J.C. Peters, T.F. Jaramillo, Benchmarking heterogeneous electrocatalysts for the oxygen evolution reaction, *J. Am. Chem. Soc.* 135 (2013) 16977–16987, <https://doi.org/10.1021/ja407115p>.
- [8] C. Li, J.B. Baek, Recent advances in noble metal (Pt, Ru, and Ir)-based electrocatalysts for efficient hydrogen evolution reaction, *ACS Omega* 5 (2020) 31–40, <https://doi.org/10.1021/acsomega.9b03550>.
- [9] J. Yu, T.A. Le, N.Q. Tran, H. Lee, Earth-abundant transition-metal-based bifunctional electrocatalysts for overall water splitting in alkaline media, *Chem. Eur. J.* 26 (2020) 6423–6436, <https://doi.org/10.1002/chem.202000209>.
- [10] S. Anantharaj, S.R. Ede, K. Sakthikumar, K. Karthick, S. Mishra, S. Kundu, Recent trends and perspectives in electrochemical water splitting with an emphasis on sulfide, selenide, and phosphide catalysts of Fe, Co, and Ni: a review, *ACS Catal.* 6 (2016) 8069–8097, <https://doi.org/10.1021/acscatal.6b02479>.
- [11] Y. Jia, K. Jiang, H. Wang, X. Yao, The role of defect sites in nanomaterials for electrocatalytic energy conversion, *Chem* 5 (2019) 1371–1397, <https://doi.org/10.1016/j.chempr.2019.02.008>.
- [12] Y. Liu, C. Xiao, P. Huang, M. Cheng, Y. Xie, Regulating the charge and spin ordering of two-dimensional ultrathin solids for electrocatalytic water splitting, *Chem* 4 (2018) 1263–1283, <https://doi.org/10.1016/j.chempr.2018.02.006>.
- [13] C. Xuan, J. Zhang, J. Wang, D. Wang, Rational design and engineering of nanomaterials derived from Prussian Blue and its analogs for electrochemical water splitting, *Chem. Asian J.* 15 (2020) 958–972, <https://doi.org/10.1002/asia.201901721>.
- [14] S. Jin, Are metal chalcogenides, nitrides, and phosphides oxygen evolution catalysts or bifunctional catalysts, *ACS Energy Lett.* 2 (2017) 1937–1938, <https://doi.org/10.1021/acseenergylett.7b00679>.
- [15] M. Sun, H. Liu, J. Qu, J. Li, Earth-rich transition metal phosphide for energy conversion and storage, *Adv. Energy Mater.* 6 (2016) 1–34, <https://doi.org/10.1002/aenm.201600087>.
- [16] S.B. Roy, S. Moon, K. Hee kim, A. Patil, M.A. Rehman, S.H. Yoo, Y. Seo, J.H. Park, K. Kang, S.C. Jun, Tuning the band (p and d) center and enhancing the active sites by nitrogen(N) doping on iridium diphosphide (IrP<sub>2</sub>) for accelerating pH-universal water electrolysis, *Appl. Catal. B Environ.* 319 (2022) 1–13, <https://doi.org/10.1016/j.apcatb.2022.121906>.
- [17] T. Xu, D. Jiao, L. Zhang, H. Zhang, D.J. Singh, J. Zhao, W. Zheng, X. Cui, Br-induced P-poor defective nickel phosphide for highly efficient overall water splitting, *Appl. Catal. B Environ.* 316 (2022), 121686, <https://doi.org/10.1016/j.apcatb.2022.121686>.
- [18] H. Zhao, Z.Y. Yuan, Design strategies of transition-metal phosphate and phosphonate electrocatalysts for energy-related reactions, *ChemSusChem* 14 (2021) 130–149, <https://doi.org/10.1002/cssc.202002103>.
- [19] P. Zhai, Y. Zhang, Y. Wu, J. Gao, B. Zhang, S. Cao, Y. Zhang, Z. Li, L. Sun, J. Hou, Engineering active sites on hierarchical transition bimetal oxides/sulfides heterostructure array enabling robust overall water splitting, *Nat. Commun.* 11 (2020) 1–12, <https://doi.org/10.1038/s41467-020-19214-w>.
- [20] A. Li, Y. Sun, T. Yao, H. Han, Earth-abundant transition-metal-based electrocatalysts for water electrolysis to produce renewable hydrogen, *Chem. Eur. J.* 24 (2018) 18334–18355, <https://doi.org/10.1002/chem.201803749>.
- [21] V.H. Hoa, D.T. Tran, S. Prabhakaran, D.H. Kim, N. Hameed, H. Wang, N.H. Kim, J. H. Lee, Ruthenium single atoms implanted continuous MoS<sub>2</sub>-Mo<sub>2</sub>C heterostructure for high-performance and stable water splitting, *Nano Energy* 88 (2021), 106277, <https://doi.org/10.1016/j.nanoen.2021.106277>.
- [22] J. Chang, Q. Lv, G. Li, J. Ge, C. Liu, W. Xing, Core-shell structured Ni<sub>1</sub>2P<sub>5</sub>/Ni<sub>3</sub>(PO<sub>4</sub>)<sub>2</sub> hollow spheres as difunctional and efficient electrocatalysts for overall water electrolysis, *Appl. Catal. B Environ.* 204 (2017) 486–496, <https://doi.org/10.1016/j.apcatb.2016.11.050>.
- [23] Y. Wang, B. Kong, D. Zhao, H. Wang, C. Selomulya, Strategies for developing transition metal phosphides as heterogeneous electrocatalysts for water splitting, *Nano Today* 15 (2017) 26–55, <https://doi.org/10.1016/j.nantod.2017.06.006>.
- [24] R. Guo, X. Lai, J. Huang, X. Du, Y. Yan, Y. Sun, G. Zou, J. Xiong, Phosphate-based electrocatalysts for water splitting: recent progress, *ChemElectroChem* 5 (2018) 3822–3834, <https://doi.org/10.1002/celec.201800996>.
- [25] V.H. Hoa, D.T. Tran, D.C. Nguyen, D.H. Kim, N.H. Kim, J.H. Lee, Molybdenum and phosphorous dual doping in cobalt monolayer interfacial assembled cobalt nanowires for efficient overall water splitting, *Adv. Funct. Mater.* 30 (2020) 1–12, <https://doi.org/10.1002/adfm.202002533>.
- [26] L. Liu, A. Corma, Confining isolated atoms and clusters in crystalline porous materials for catalysis, *Nat. Rev. Mater.* 6 (2021) 244–263, <https://doi.org/10.1038/s41578-020-00250-3>.
- [27] Y. Deng, L. Yang, Y. Wang, L. Zeng, J. Yu, B. Chen, X. Zhang, W. Zhou, Ruthenium nanoclusters anchored on cobalt phosphide hollow microspheres by green phosphating process for full water splitting in acidic electrolyte, *Chin. Chem. Lett.* 32 (2021) 511–515, <https://doi.org/10.1016/j.ccllet.2020.03.076>.
- [28] J.N. Tiwari, S. Sultan, C.W. Myung, T. Yoon, N. Li, M. Ha, A.M. Harzandi, H. J. Park, D.Y. Kim, S.S. Chandrasekaran, W.G. Lee, V. Vij, H. Kang, T.J. Shin, H. S. Shin, G. Lee, Z. Lee, K.S. Kim, Multicomponent electrocatalyst with ultralow Pt loading and high hydrogen evolution activity, *Nat. Energy* 3 (2018) 773–782, <https://doi.org/10.1038/s41560-018-0209-x>.
- [29] Q. Hu, K. Gao, X. Wang, H. Zheng, J. Cao, L. Mi, Q. Huo, H. Yang, J. Liu, C. He, Subnanometric Ru clusters with upshifted D band center improve performance for alkaline hydrogen evolution reaction, (n.d.) 1–10, <https://doi.org/10.1038/s41467-022-31660-2>.

- [30] K. Jiang, M. Luo, M. Peng, Y. Yu, Y.R. Lu, T.S. Chan, P. Liu, F.M.F. de Groot, Y. Tan, Dynamic active-site generation of atomic iridium stabilized on nanoporous metal phosphides for water oxidation, *Nat. Commun.* 11 (2020) 1–9, <https://doi.org/10.1038/s41467-020-16558-1>.
- [31] Z. Lei, W. Cai, Y. Rao, K. Wang, Y. Jiang, Y. Liu, X. Jin, J. Li, Z. Lv, S. Jiao, W. Zhang, P. Yan, S. Zhang, R. Cao, Coordination modulation of iridium single-atom catalyst maximizing water oxidation activity, *Nat. Commun.* 13 (2022) 1–10, <https://doi.org/10.1038/s41467-021-27664-z>.
- [32] C. Dong, Y. Li, D. Cheng, M. Zhang, J. Liu, Y.G. Wang, D. Xiao, D. Ma, Supported metal clusters: fabrication and application in heterogeneous catalysis, *ACS Catal.* 10 (2020) 11011–11045, <https://doi.org/10.1021/acscatal.0c02818>.
- [33] Z. Chen, X. Duan, W. Wei, S. Wang, B.J. Ni, Iridium-based nanomaterials for electrochemical water splitting, *Nano Energy* 78 (2020), 105270, <https://doi.org/10.1016/j.nanoen.2020.105270>.
- [34] A. Irshad, N. Munichandraiah, High catalytic activity of amorphous Ir-Pi for oxygen evolution reaction, *ACS Appl. Mater. Interfaces* 7 (2015) 15765–15776, <https://doi.org/10.1021/acscami.5b02601>.
- [35] Z. Yu, Y. Li, A. Torres-Pinto, A.P. LaGrow, V.M. Diaconescu, L. Simonelli, M. J. Sampaio, O. Bondarchuk, I. Amorim, A. Araujo, A.M.T. Silva, C.G. Silva, J. L. Faria, L. Liu, Single-atom Ir and Ru anchored on graphitic carbon nitride for efficient and stable electrocatalytic/photocatalytic hydrogen evolution, *Appl. Catal. B Environ.* 310 (2022), <https://doi.org/10.1016/j.apcatb.2022.121318>.
- [36] S. Li, Y. Xu, Y. Chen, W. Li, L. Lin, M. Li, Y. Deng, X. Wang, B. Ge, C. Yang, S. Yao, J. Xie, Y. Li, X. Liu, D. Ma, Tuning the selectivity of catalytic carbon dioxide hydrogenation over iridium/cerium oxide catalysts with a strong metal-support interaction, *Angew. Chem.* 129 (2017) 10901–10905, <https://doi.org/10.1002/ange.201705002>.
- [37] R. Fan, Q. Mu, Z. Wei, Y. Peng, M. Shen, Atomic Ir-doped NiCo layered double hydroxide as a bifunctional electrocatalyst for highly efficient and durable water splitting, *J. Mater. Chem. A* 8 (2020) 9871–9881, <https://doi.org/10.1039/d0ta03272g>.
- [38] V.H. Hoa, S. Prabhakaran, K.T. Nhi Le, D.H. Kim, A single atom Ir doped heterophase of a NiMoP-NiMoPxOy ultrathin layer assembled on CNTs-graphene for high-performance water splitting, *J. Mater. Chem. A* 10 (2022) 14604–14612, <https://doi.org/10.1039/d2ta03325a>.
- [39] F. Chen, B. Zhao, M. Sun, C. Liu, Y. Shi, Y. Yu, B. Zhang, Mechanistic insight into the controlled synthesis of metal phosphide catalysts from annealing of metal oxides with sodium hypophosphite, *Nano Res.* (2022), <https://doi.org/10.1007/s12274-022-4489-x>.
- [40] L. Liu, A. Corma, Evolution of isolated atoms and clusters in catalysis, *Trends Chem.* 2 (2020) 383–400, <https://doi.org/10.1016/j.trechm.2020.02.003>.
- [41] C. Lu, S. Liu, F. Zhang, Y. Su, X. Zou, Z. Shi, G. Li, X. Zhuang, An interfacial engineering approach towards two-dimensional porous carbon hybrids for high performance energy storage and conversion, *J. Mater. Chem. A* 5 (2017) 1567–1574, <https://doi.org/10.1039/c6ta09278k>.
- [42] D. Kobashi, S. Kohara, J. Yamakawa, A. Kawahara, Structure d'un Diphosphate Synthétique de Cobalt: Co2P2O7, *Acta Crystallogr. Sect. C: Cryst. Struct. Commun.* 53 (1997) 1523–1525, <https://doi.org/10.1107/S0108270197006689>.
- [43] D.T. Tran, H.T. Le, T.L. Luyen Doan, N.H. Kim, J.H. Lee, Pt nanodots monolayer modified mesoporous Cu@Cu x O nanowires for improved overall water splitting reactivity, *Nano Energy* 59 (2019) 216–228, <https://doi.org/10.1016/j.nanoen.2019.02.050>.
- [44] H.S. Oh, H.N. Nong, T. Reier, M. Gliche, P. Strasser, Oxide-supported Ir nanodendrites with high activity and durability for the oxygen evolution reaction in acid PEM water electrolyzers, *Chem. Sci.* 6 (2015) 3321–3328, <https://doi.org/10.1039/c5sc00518c>.
- [45] C.C. Shan, D.S. Tsai, Y.S. Huang, S.H. Jian, C.L. Cheng, Pt-Ir-O2NT thin-wall electrocatalysts derived from IrO 2 nanotubes and their catalytic activities in methanol oxidation, *Chem. Mater.* 19 (2007) 424–431, <https://doi.org/10.1021/cm062085u>.
- [46] S.R. Shieh, T.S. Duffy, Raman spectroscopy of (formula presented) at high pressures: implications for amorphization and hydrogen repulsion, *Phys. Rev. B - Condens. Matter Mater. Phys.* 66 (2002) 1–8, <https://doi.org/10.1103/PhysRevB.66.134301>.
- [47] M. Harcharras, A. Ennaciri, F. Capitelli, G. Mattei, Vibrational spectra and thermal dehydration of Co2P 2O7-6H2O diphosphate, *Vib. Spectrosc.* 33 (2003) 189–196, <https://doi.org/10.1016/j.vibspec.2003.09.001>.
- [48] X. Yu, J. Zhao, M. Johnsson, Interfacial engineering of nickel hydroxide on cobalt phosphide for alkaline water electrocatalysis, *Adv. Funct. Mater.* 31 (2021), <https://doi.org/10.1002/adfm.202101578>.
- [49] V.H. Hoa, D.T. Tran, H.T. Le, N.H. Kim, J.H. Lee, Hierarchically porous nickel-cobalt phosphide nanoneedle arrays loaded micro-carbon spheres as an advanced electrocatalyst for overall water splitting application, *Appl. Catal. B Environ.* 253 (2019), <https://doi.org/10.1016/j.apcatb.2019.04.017>.
- [50] A.W. Burns, K.A. Layman, D.H. Bale, M.E. Bussell, Applied catalysis a: general understanding the relationship between composition and hydrodesulfurization properties for cobalt phosphide catalysts 343 2008 68 76 doi: 10.1016/j.apcata.2008.03.022.
- [51] L. Wu, F. Zhang, S. Song, M. Ning, Q. Zhu, J. Zhou, G. Gao, Z. Chen, Q. Zhou, X. Xing, T. Tong, Y. Yao, J. Bao, L. Yu, S. Chen, Z. Ren, Efficient alkaline water/seawater hydrogen evolution by a nanorod-nanoparticle-structured Ni-MoN catalyst with fast water-dissociation kinetics, *Adv. Mater.* 34 (2022) 1–12, <https://doi.org/10.1002/adma.202201774>.
- [52] Q. Wang, Z. Zhang, C. Cai, M. Wang, Z.L. Zhao, M. Li, X. Huang, S. Han, H. Zhou, Z. Feng, L. Li, J. Li, H. Xu, J.S. Francisco, M. Gu, Single iridium atom doped Ni2P catalyst for optimal oxygen evolution, *J. Am. Chem. Soc.* 143 (2021) 13605–13615, <https://doi.org/10.1021/jacs.1c04682>.
- [53] Z. Wang, Z. Lin, P. Diao, Hybrids of iridium-cobalt phosphates as a highly efficient electrocatalyst for the oxygen evolution reaction in neutral solution, *Chem. Commun.* 55 (2019) 3000–3003, <https://doi.org/10.1039/c8cc10278c>.
- [54] C. Wang, P. Zhai, M. Xia, Y. Wu, B. Zhang, Z. Li, L. Ran, J. Gao, X. Zhang, Z. Fan, L. Sun, J. Hou, Engineering lattice oxygen activation of iridium clusters stabilized on amorphous bimetal borides array for oxygen evolution reaction, *Angew. Chem. - Int. Ed.* 60 (2021) 27126–27134, <https://doi.org/10.1002/anie.202112870>.
- [55] X. Li, W. Liu, M. Zhang, Y. Zhong, Z. Weng, Y. Mi, Y. Zhou, M. Li, J.J. Cha, Z. Tang, H. Jiang, X. Li, H. Wang, Strong metal-phosphide interactions in core-shell geometry for enhanced electrocatalysis, *Nano Lett.* 17 (2017) 2057–2063, <https://doi.org/10.1021/acs.nanolett.7b00126>.
- [56] L. Guo, J. Chi, J. Zhu, T. Cui, J. Lai, L. Wang, Dual-doping NiMoO4 with multi-channel structure enable urea-assisted energy-saving H2 production at large current density in alkaline seawater, *Appl. Catal. B Environ.* 320 (2023), 121977, <https://doi.org/10.1016/j.apcatb.2022.121977>.
- [57] B. Wang, F. Zhang, Main descriptors to correlate structures with the performances of electrocatalysts, *Angew. Chem. - Int. Ed.* 61 (2022), <https://doi.org/10.1002/anie.202111026>.
- [58] S. Drespe, F. Dionigi, M. Klingenhof, P. Strasser, Direct electrolytic splitting of seawater: opportunities and challenges, *ACS Energy Lett.* 4 (2019) 933–942, <https://doi.org/10.1021/acscenergylett.9b00220>.
- [59] P.K.L. Tran, D.T. Tran, D. Malhotra, S. Prabhakaran, D.H. Kim, N.H. Kim, J.H. Lee, Highly effective freshwater and seawater electrolysis enabled by atomic Rh-modulated Co-CoO lateral heterostructures, *Small* 17 (2021) 1–13, <https://doi.org/10.1002/smll.202103826>.
- [60] H. Song, S. Luo, H. Huang, B. Deng, J. Ye, Solar-driven hydrogen production: recent advances, challenges, and future perspectives, *ACS Energy Lett.* 7 (2022) 1043–1065, <https://doi.org/10.1021/acscenergylett.1c02591>.
- [61] J. Jia, L.C. Seitz, J.D. Benck, Y. Huo, Y. Chen, J.W.D. Ng, T. Bilir, J.S. Harris, T. F. Jaramillo, Solar water splitting by photovoltaic-electrolysis with a solar-to-hydrogen efficiency over 30%, *Nat. Commun.* 7 (2016) 1–6, <https://doi.org/10.1038/ncomms13237>.